EFFECT OF FROST FORMATION ON HEAT TRANSFER: EXPERIMENTAL INVESTIGATION AND NUMERICAL MODEL DEVELOPMENT

A Thesis

by

Alper Saygin

Submitted to the
Graduate School of Sciences and Engineering
In Partial Fulfillment of the Requirements for
the Degree of

Master of Science

in the
Department of Mechanical Engineering

Özyeğin University
June 2023

EFFECT OF FROST FORMATION ON HEAT TRANSFER: EXPERIMENTAL INVESTIGATION AND NUMERICAL MODEL DEVELOPMENT

Approved by:

Assist. Prof. Altuğ Melik Başol,
Advisor
Department of Mechanical Engineering
Özyeğin University

Assist. Prof. Hande Öztürk
Department of Mechanical Engineering
Ozyegin University

Prof. Mehmet Arık,
Co-Advisor
Department of Mechanical Engineering
Ozyegin University

Assoc. Prof. Özgür Ertunç
Department of Mechanical Engineering
Ozyegin University

Date Approved: 7 June 2023

Lorenzo Cremaschi, Ph.D.
Professor, Department of Mechanical Engineering
Auburn University

To My Family...

ABSTRACT

Water molecules freeze when the temperature drops below the triple point. This phase change process results in the formation of ice crystals. With air filling the gaps between the growing ice columns, together this porous medium known as ”frost”. The accumulation of frost creates a thermal barrier across a surface due to the low thermal conductivity of the frost layer. This phenomenon is commonly observed in heating, ventilation, and air-cooling applications, such as evaporators in household refrigerators, air source heat pumps, and aircraft precoolers. Therefore, it is crucial to investigate the dynamic heat transfer rates across surfaces operating under frosting conditions to assess their performance and develop defrosting strategies. In this thesis study, the effect of frosting on heat transfer is investigated experimentally, and the gathered data is utilized in a numerical frosting model development. A large number of experiments are performed by altering the parameters of free stream air velocity, relative humidity, and cold plate temperature. Frosting impact on heat transfer rate is measured through a high-precision thin film heat flux sensor. Accordingly, heat flow is significantly obstructed due to frosting in time. The rate of decrease in the heat flux is not found to be constant over time but shows a decreasing trend. Additionally, an enhancement in the heat transfer is reported during the early stage of frost formation under certain environmental conditions, due to the increase in effective heat transfer area induced by ice crystals and the corresponding increase in latent heat generation. The densification of the frost layer and its effect on the total thermal resistance is discussed. Based on the convective heat and mass transfer balance over the frost layer, frost surface temperature was predicted. A correlation for estimating the heat transfer decrease during frosting is proposed via non-dimensional numbers. The gathered empirical data is utilized to establish a robust numerical model. An Eulerian-Eulerian multiphase approach is followed to model humid air and frost phases separately. Heat flux during a dynamic frosting process is also calculated during the frosting simulations, and validation of the proposed model is done over the experimental heat transfer measurements. Frost accumulation on the cold surface is modeled with an empirical mass source term. Model constants are tuned in a systematic way using experimental heat flux and frost thickness data. A velocity dependent model constant is introduced into the mass source term. The heat flux rise observed experimentally at the initial stages of the frosting could be captured with the use of the velocity dependent model constant and the addition of this term considerably improves the accuracy of the frost model at the initial stages of frosting. The developed numerical model is tested with three different frost thermal conductivity models. Using the thermal conductivity of solid ice for the frost thermal conductivity results in the most accurate prediction at the early stages of the frost growth process indicating a rather column-wise vertical growth of ice crystals with very low lateral branching. However, the overprediction of the numerical heat flux with the thermal conductivity of solid ice points out a decrease in the thermal conductivity of the newly added frost layers indicating a more pronounced lateral branching of ice crystals within the frost layer. The effect of the diffusion coefficient of the water vapor in humid air on frosting is also investigated. An artificial increase in the diffusion coefficient improves the accuracy of the heat flux prediction of the model at the initial stages of frosting which might indicate an eddy-driven enhanced mixing in the boundary layer which might not be captured in the laminar flow model. Finally, the developed numerical model is also tested on another scenario where surface temperature is set differently.

ÖZETÇE

Sıcaklık üçlü noktanın altına düştüğünde su molekülleri donar ve bu faz değişim süreci nedeniyle buz kristalleri oluşur. Bir yüzey üzerinde büyüyen buz sütunları arasındaki porlarda hava yer alır. ”Karlanma” terimi, buz kristallerinden oluşan gözenekli ortamı ve buz kristalleri arasında sıkışan havayı ifade eder. Kar tabakası çok düşük ısı iletkenliğine sahip olduğundan, soğutulmuş yüzeylerde kar birikmesi yüzey ile hava arasında termal bariyer oluşturur. Bu, bir yüzeyin çevredeki ortamla ısı alışverişi yeteneğini kaybetmesine neden olur. Bu sorun genellikle bir dizi ısıtma, havalandırma ve hava soğutma uygulamasında görülür. Tipik bir ev tipi buzdolabındaki buharlaştırıcılar, hava kaynaklı ısı pompaları ve uçak ön soğutucuları, karlanmaya eğilimli ısı eşanjörlerinden bazılarıdır. Bu nedenle, etkili kar çözme stratejileri geliştirmek için karlanma koşullarında çalışan bir yüzeydeki zamana bağlı ısı transfer hızlarını araştırmak önemlidir. Bu tez çalışmasında, karlanmanın ısı transferi üzerindeki etkisi deneysel olarak araştırılmış ve toplanan veriler sayısal bir karlanma modeli geliştirmede kullanılmıştır. Serbest akışlı hava hızı, bağıl nem ve soğuk plaka sıcaklığı parametreleri değiştirilerek çok sayıda deney gerçekleştirilir. Kar tabakasının ısı transfer hızı üzerindeki etkisi, yüksek hassasiyetli ince film ısı akısı sensörü ile ölçülür. Buna göre, zaman içinde karlanma nedeniyle ısı akışı önemli ölçüde engellendi. Isı akışındaki azalma oranının zaman içinde sabit olmadığı, ancak azalan bir eğilim gösterdiği görülmüştür. Ayrıca, buz kristallerinin neden olduğu etkili ısı transfer alanındaki artış ve buna bağlı olarak gizli ısı üretimindeki artış nedeniyle, belirli çevresel koşullar altında kar oluşumunun erken aşamasında ısı transferinde bir artış bildirilmiştir. Kar tabakasının yoğunlaşması ve toplam ısıl direnç üzerindeki etkisi tartışıldı. Kar tabakası üzerindeki konvektif ısı ve kütle transfer dengesine

dayanarak, kar yüzey sıcaklığı tahmin edildi. Karlanma sırasında ısı transferindeki azalmayı tahmin etmek için boyutsuz sayılarla bir korelasyon önerilmektedir. Ampirik veriler, sağlam bir sayısal model oluşturmak için kullanılır. Nemli hava ve don fazlarını ayrı ayrı modellemek için Euler-Euler çok fazlı bir yaklaşım izlenir. Bir buzlanma işlemi sırasındaki ısı akışı, karlanma simülasyonları sırasında da hesaplanır ve önerilen modelin deneysel ısı transferi ölçümleri üzerinden doğrulanması yapıldı. Soğuk yüzeydeki kar birikimi, ampirik bir kütle kaynağı terimi ile modellenmiştir. Model sabitleri, deneysel ısı akısı ve kar kalınlığı verileri kullanılarak sistematik bir şekilde ayarlandı. Kütle kaynağı terimine hıza bağlı bir model sabiti eklenir. Karlanmanın ilk aşamalarında deneysel olarak gözlemlenen ısı akısı artışı, hıza bağlı model sabiti kullanılarak yakalanabilir ve bu terimin eklenmesi, karlanamnın ilk aşamalarında don modelinin doğruluğunu önemli ölçüde iyileştirdi. Geliştirilen sayısal model üç farklı kar ısı iletkenlik modeli ile test edilmiştir. Kar termal iletkenliği için katı buzun termal iletkenliğinin kullanılması, kar büyüme sürecinin erken aşamalarında, çok düşük yanal dallanma ile buz kristallerinin oldukça kolon bazında dikey büyümesini gösteren en doğru tahminle sonuçlandı. Bununla birlikte, sayısal ısı akısının katı buzun termal iletkenliği ile aşırı tahmin edilmesi, yeni eklenen kar katmanlarının termal iletkenliğinde, kar katmanı içinde buz kristallerinin daha belirgin bir yanal dallanmasını gösteren bir azalmaya işaret eder. Nemli havadaki su buharının difüzyon katsayısının buzlanmaya etkisi de araştırılmıştır. Difüzyon katsayısındaki yapay bir artış, buzlanmanın ilk aşamalarında modelin ısı akısı tahmininin doğruluğunu iyileştirdi; bu, sınır tabakasında laminer akış modelinde yakalanamayabilecek girdapla çalışan gelişmiş bir karışımı gösterebilir. Son olarak, geliştirilen sayısal model, yüzey sıcaklığı -30 ° C'de tutulan başka bir senaryo üzerinde de test edilir. Sayısal simülasyonların ayrıntılı analizi, -20 °C'de yüzeyde oluşan kargözenekliliğine kıyasla -30 °C'de yüzey sıcaklığına sahip bir yüzeyde daha gözenekli bir don tabakası oluştuğunu gösterdi.

ACKNOWLEDGEMENTS

First and foremost, I would like to thank my advisor Dr. Altug Basol for all of his guidance and effort throughout my thesis study. I can't put into words how grateful I am for everything he taught me. He became a role model to me with his intellectual approach to engineering problems. Also, his commitment to conducting superior research served as a great inspiration source, and greatly helped me to build self-confidence to always aim higher. The outcome of this thesis study couldn't have been improved that much without his mentorship. I always considered myself very lucky and special that I had the opportunity to conduct research under his supervision.

I would like to also express my greatest appreciation to my co-advisor Prof. Mehmet Arik for his support and trust in me. He has endless motivation to do research and was always eager to give his best whenever I need. Also, I am very thankful to him because of the vision he had portrayed to me. I have gained very valuable experience during my research studies with him. I am very grateful for his trust and all responsibilities he has given me, which helped me develop professionally.

I would like to use these lines to thank all of my colleagues in the Heat Transfer Lab. I would like to recognize Ceyhun Topal, Onuralp Işıl, Hamza Ourabi, Ceren Cengiz, Mohammad Azarifar, Enes Öksüz, Dr. Mete Budaklı, and all other great people I had the pleasure of meeting and collaborating with. I am grateful that I spent my years there.

Especially, I would like to extend my sincere thanks to Mete Muslu for his continuous support, help, advice, and all the valuable experiences he has shared with me throughout the years. I would like to also thank to my dearest friend Batuhan Bayır, for all scientific discussions we had over partial differential equations and mathematics, which I enjoyed a lot and kindled my curiosity. Lastly, I would be remiss in not mentioning my colleague Tolga Emir, who always became a great company over the years.

Finally, my deepest gratitude is to my parents Cemal and Gülşen Saygın, to my dearest brother Caner Saygın and his wife Didem Saygın. They always believed in me and encouraged me to pursue my dreams. I am deeply indebted to them for getting me to where I am today.

TABLE OF CONTENTS

LIST OF TABLES

LIST OF FIGURES

C_d : Drag coefficient

D : Diffusion coefficient

f : Friction coefficient

h : Enthalpy

h_a : Convective heat transfer coefficient [W/$m^2 - C$]

h_m : Convective mass transfer coefficient [kg/$m^2 - s$]

$h_s ub$: Sublimation enthalpy [kJ/kg]]

k : Thermal conductivity

K : Momentun exchange coefficient

L : Latent heat of deposition [kJ/kg]

$\dot{m}$: Mass Source Term

P : Pressure [Pa]

P_c : Pressure of the Cell[Pa]

P_{ref} : Reference Pressure [Pa]

R : Ideal Gas Constant

R_{va} : Ideal Gas Constant of Water Vapor

S : Source Term

S_m : Mass Source Term

S_q : Momentum Source Term

S_h : Energy Source Term

t : time [min]

T : Temperature [$^{\circ}C$]

T_a : Ambient Air Temperature [$^{\circ}C$]

T_{ha} : Temperature of the humid air phase [$^{\circ}C$]

T_{fs} : Frost surface temperature [$^{\circ}C$]

T_i	:	Temperature of ice phase [$°C$]
T_{ref}	:	Reference temperature [$°C$]
T_w	:	Cold wall temperature [$°C$]
w	:	Humidity Ratio [kg/kg]
u	:	x−component of the velocity vector [m/s]
v	:	y−component of the velocity vector [m/s]
V	:	Velocity Vector [m/s]
x	:	x - coordinate
y	:	y - coordinate
w	:	Water vapor mass fraction [kg/kg]
q"	:	Heat Flux [W/m^2]

Greek Letters

α	:	Volume fraction
κ	:	Dimensionless velocity factor
δ	:	Frost thickness [mm]
Δ	:	Difference
ρ	:	Density [kg/m^3]
τ	:	Time relaxation constant [s^{-1}]
$\overline{\overline{\tau}}$	:	Stress tensor [s^{-1}]
ϕ	:	Independent variable

Dimensionless Numbers

Fo	:	Fourier Number
Le	:	Lewis Number
Pr	:	Prandtl Number
Re	:	Reynolds Number

CHAPTER I

INTRODUCTION

Ice formation is a phase change process during which water molecules freeze, generally over a substrate, and crystals stems. Between the gaps of the growing ice columns over a surface, air molecules reside. Together, the porous media consisting of ice crystals and trapped air in between is called as frost layer. This process is driven by mainly supersaturation and temperature.

Air has the capacity to carry moisture at each finite temperature, making it humid. Accordingly, the maximum amount of humidity can be stored by air at any temperature is called as saturation level. This level has a dependency on temperature, which is shown in Figure 1. Growth of the ice crystals continues as long as excess humidity presents in the surrounding air. Induced by the drop in temperature ΔT, this excess amount of humidity is called as supersaturation, Δw, being the main driver of frosting phase change process. The another must for frosting to occur is, surface temperature must be below the triple point temperature of water.

Frosting is a widely encountered phenomenon in air conditioning, refrigeration, and cryogenics industries. Humidity content of air deposits over refrigerated surfaces, leading to formation and continual growth of a frost layer. This process might adversely affect the performance of thermal devices, such as refrigerators, compact heat exchangers and heat pumps, since accumulated frost over a surface act as an insulator and prevent heat from being transferred between the surface and its surroundings. Eventually, it leads to a substantial loss in heat transfer.

Frosting process includes both heat and mass transfer mechanisms simultaneously. Air velocity, surface temperature, air temperature and air humidity level are the

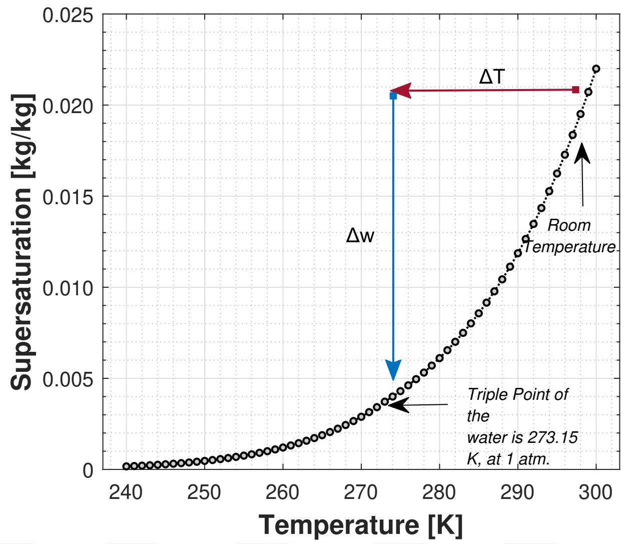

Figure 1: Mass fraction of water vapor at the saturation level with respect to different temperatures.

most fundamental parameters affecting the rates of these mechanisms greatly, such that heat transfer transparency of frost layer changes. Figure 2 depicts the frosting mechanism. Flowing humid air carries water in its vapor form, which deposits over the cold surface and forms a frost. Through the course of the process, some portion of the incoming water vapor contributes to the growth of the frost layer, whose effect is seen as a frost thickness rise. The rest of the water vapor diffuses towards to the frosted surface, and de-sublimates inside of the frost layer, leading to a frost densification. Across a frost layer, two main sources of the heat flow are sensible heat and latent heat. Sensible heat is due to finite temperature difference between streaming air and frost front. Moreover, latent heat is released due to desublimation process contributes to the total heat flux. It is heat rejected due to bond formation between water vapor molecules and proportionally related to amount of mass generation.

Dynamic heat transfer rates across a surface over which frosting occurs is a need-to-know quantity to aid better designs and develop defrosting strategies. Frost is a porous medium, and each frost layer exhibit different characteristic in terms of heat transparency. Air velocity, cold surface temperature, air temperature and air

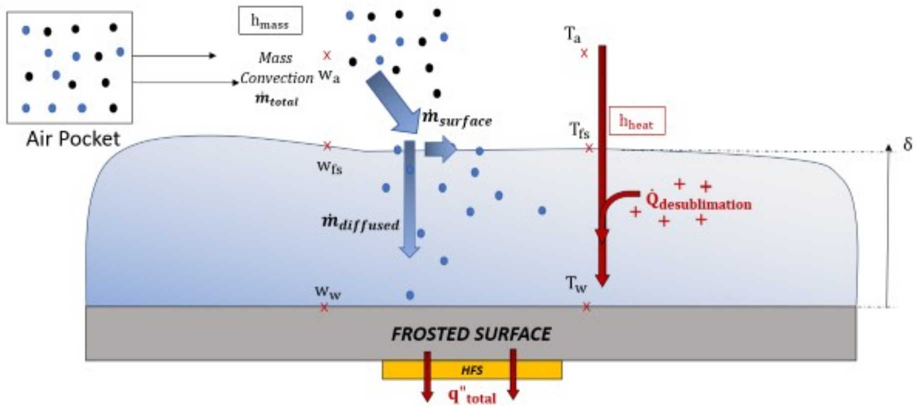

Figure 2: Description of frost formation process on the test surface.

humidity level are the most fundamental parameters affecting frosting rate and its thermal properties. Therefore, many studies have been conducted to assess their impact on thermal characteristics of a frost layer. Overall, to calculate heat transfer through a frost layer, a direct measurement of heat transfer rate could be possible by employing a heat flux sensor or series of thermocouples. Generally, two or more thermocouples are positioned adjacent to each other with a finite distance between them inside a conductive material. Then, heat flux can be calculated through temperature differences recorded over time. Alternatively determining frost layer thermal conductivity, surface temperature and thickness might be sufficient. Then, heat flux could be derivable based on Fourier's law of conduction.

An extensive amount of semi-empirical and theoretical models was presented to determine frost thermal conductivity to calculate heat transfer rate. It is an integral variable, and extremely hard to determine accurately. Perhaps as the most simplistic approach, many authors defined effective thermal conductivity as a function of frost density or porosity. In one of the earliest papers, the relationship between the frost density and thermal conductivity is first reported by Yonko and Sepsy [2]. They defined the frost thermal conductivity as a second order polynomial function of frost density. In the later studies, it was hypothesized for the first time that the conduction path of the heat alters based on the crystal growth directions. Auracher [3], and Hayashi et al. [4] further improved the accuracy of previous density-based correlations by including the frost growth patterns in serial and parallel directions. The correlations of the prementioned authors dictate that thermal conductivity increases as the frost density increases. It is not surprising that a denser frost layer facilitates better heat flow, since the thermal conductivity of ice is approximately 100 times bigger than that of air's. The relationship between the density and conductivity is not yet that simple, and more comprehensive analysis could be employed by contributing the ice crystals shape and orientations. For that purpose, Na and Webb [5] incorporated the ice crystal shapes in their thermal conductivity correlation. Kobayashi's Chart was utilized to classify ice crystal shapes in the study, and model development was done based on existence of supersaturated conditions at the frost surface. When compared with the published data, their proposed correlation showed a good prediction ability of 80 %, when the plate temperature spans from -4 to -27 °C. In a study, Wu et al. [1] conducted experimental research, and microscopically observed ice crystal growth process in the early stage of frosting. Based on that they mapped the frost crystal types concerning different supersaturation degrees and plate temperatures. Their proposed map was heavily utilized by the future studies and further facilitated the inclusion of ice crystal shapes for the estimation of frost thermal conductivity. In a more comprehensive study, Negrelli et al. [6] gathered 183 available data points in the literature and proposed an advanced frost thermal conductivity correlation based on frost layer's internal structure, with a high estimation accuracy of 83 %. They included the effect of ice crystals growth direction to frost thermal conductivity. It was shown in their study that frost layer thermal conductivity deviates from the parallel only orientation of ice crystals, as the surface temperature increases. Accordingly, it was concluded that it may yield a great error to treat frost layer thermal conductivity as a simple geometric average between ice and air or accepting parallel only orientation for the known same frost porosity levels. The real frost thermal conductivity value stayed in between these two regimes and must be tuned with the factors given in the study for different plate temperatures. In a more recent study, Li et al. [7] carried out a similar study to estimate thermal conductivity by incorporating the ice crystal configuration and morphology. Their main improvement against the correlation put forward by Negrelli et al. [6] is the better prediction ability of thermal conductivity at frost densities lower than 125 kg/m^3.

Another requisite to determine the heat flux through a frost layer is the estimation frost surface temperature. It is determined either by experimental measurements or proposed models. In their studies Lee et al. [8, 9] utilized an IR thermal camera to detect frost surface temperature over a period of time. According to measurements, the most substantial rise in frost surface temperature occurs in the early stages of frost formation. Furthermore, frost surface temperature was found to be higher as the velocity of the air stream was elevated. Their measurements were used as a reference for most of the future studies. Accordingly, based on this experimental data, Yun et al. [10] proposed a mathematical model to capture frost surface temperature over time. In their model, the rough nature of frost-air interface was also included to aid the accuracy. Yet, their proposed model deviates from the Lee's measurements, especially at the initial duration of frosting. Similarly, Kandula [11] carried out an extensive analytical study to calculate frost properties. Accordingly, a non-linear increasing trend of frost surface temperature was denoted. However, his calculations of frost surface temperature also show poor agreement with the Lee's experimental measurements, especially for the lower air velocities and relative humidity. At that point, it is questionable that IR thermal measurement of a frost surface temperature could not be achievable with a reasonably low error due to the porous nature of air-frost interface. The emissivity of the frost surface also poses an added uncertainty since it is not a solid and smooth surface. Overall, indirect measurements done by an IR camera might not be able to capture the exact location of air-frost interface. When it comes to direct measurements, (e.g thermocouples or thermistors), the tip of the measurement tool either breaks or melts the frost layer since the ice crystals are extremely fragile. Therefore, probably the detailed semi-analytical correlations could be more reliable for the estimation of frost surface temperature. The most accurate method to capture frost surface temperature employed in the literature can still be mentioned as Holographic Interferometry. It is rarely used for that purpose since it is expensive and hard to implement. Hao et al. [12] made use of this technique in their research . One important conclusion of this study shows that, frost surface temperature approaches the similar values in time regardless of cold plate temperature.

Lastly, thickness of a frost layer in different environmental conditions and its growth rate in time was another concern for researchers. It has been reported in many studies that frost thickness increases as the cold surface temperature decreases [13–19]. This trend has been well accepted in the open literature. However, when it comes to the effect of air velocity, still contradictions exist. Cheng et al. [16] performed an experimental analysis over spatial variation of thickness along the frost layer. They reported that the thickest region is most generally at the leading edge, since heat and mass transfer processes are more abundant in there. It was stated in the study that, elevation of air velocity results in a thicker frost at the leading edge, since more crystal branches emerge. Similarly, Lee et al. [8] provided data reporting that higher air velocities promote thicker frost layers. It was given in the experimental data that, at least 10 % increase in thickness was measured when doubling the air velocity. In contrast, several studies stated that an increase in air velocity does not favor thicker frost layers. Instead, it leads to a higher frost surface temperature and a denser frost layer due to high heat and mass transfer coefficients. In one of the early studies, Ostin et al. [13] reported negligible enhancement of the frost thickness with increase in air velocity. Likewise, Sahin et al. [14] provided experimental data in a broader range of Re and concluded that frost height insensitive to air velocity changes. It was hypothesized in the study that, rising the air velocity primarily affects the frost density, rather than thickness. O'Neal [20] put forward a critical Re value of 15900, above which frost thickness shows no dependency to Re. Below that limit, frost thickness increases as the Re number becomes higher. Huang et al. [18] proposed supporting experimental data by reporting a weak dependency of frost thickness to Re number up to 37400. In a more recent, Lee et al. [21] conducted a frosting study where frost formation is primarily driven by direct deposition, which is favorable in plate temperatures close to cryogenic conditions. It was also seen that an increase in air velocity did not promote a thicker frost layer. Overall, the effect of air velocity on the frost thickness remains unclear and more experimental data is required to reach a conclusive argument.

There have been many 1-D mathematical models developed in the past to model frost deposition. These models focus on one directional growth rate of the frost layer and change in its thermal properties, considering various parameters of air temperature, humidity velocity, and frosted surface temperature. These factors affect the frost layer's thermal properties and lead to different frost characteristics. One of the earliest 1-D mathematical frost models was put forward by Jones et al. [22]. In that model, considering the frost layer as a porous medium and solving the mass diffusion across the structure, frost thickness growth was estimated in time. A parametric study was also conducted to calculate the frost thicknesses under different operating conditions. In a theoretical study, Lee et al. [8] calculated the frost surface temperature by establishing heat and mass transfer balance over the frost surface and estimated the frosting rate. Although most of the models [8, 11, 22, 23] assumed that water vapor is saturated across a frost layer, in their studies, Na and Webb [24] hypothesized that water vapor must be in a supersaturated state at the frost surface. Using this conclusion, they put forward a mathematical model and calculated frost density and thickness. Denoting a large frosting rate difference between the two assumptions about the water vapor saturation state, they also proposed an improved frost thermal conductivity correlation [5]. Kandula [11] carried out a detailed mathematical analysis to further estimate the heat flux and surface temperature of the frost layer. Later, an analytical solution was derived by Hermes [23] to solve frost growth and densification over a flat plate. The developed model was used to calculate frost thickness, reporting a good fit with the experimental findings.

Recently, 2D and 3D numerical frost modeling also gained significance and became the focus of researchers, especially with the greater availability of commercial CFD software packages. The main advantage of using computational fluid dynamics to model frosting is, the local values of temperature, volume fraction, density, and thermal conductivity could be calculated throughout an entire frost layer. The devised models in the past were generally applied over the source terms existing at the right-hand side of the conservation equations. This source term driven phase transfer approach was heavily utilized by previous researchers, and many physics-based phase transfer models were proposed and tested in the open literature. In one of the earliest 2D computational studies, Cui et al. [25] proposed a phase transfer model between water vapor and ice based on the classical nucleation theory. In their model, the mass source term was derived such that both ice crystal nucleation and growth processes are considered. The validation of their proposed model was done over the average frost thickness data obtained from the experimental results. They further employed their frosting model to estimate the frost growth inside a fin-and-tube heat exchanger [26]. The research carried out the first 3D frosting simulation in the literature. Accordingly, a rise in frost thickness, and subsequent increase in pressure drops, and a decrease in the air-side heat transfer coefficient were the parameters considered in the numerical simulations. A denser frost layer was reported towards the leading-edge direction with the utilized mass transfer mechanism. The model sensitivity was also tested under different air velocities, surface temperatures, relative humidity inlets, and fin pitches. However, although the findings of this research show logical trends for heat transfer and pressure drop calculations, the study lacks experimental validation, which jeopardizes the results. In another study, Kim et al. [27] proposed a mass transfer model based on mass flux towards the frost layer and modified Sauter mean diameter. The model validation was done over the experimental frost thickness data, and correlation-based frost density and cold surface temperature calculations. The proposed model estimated the increase in the frost thickness closely with the experimental measurements, under different cold surface temperatures and air velocities. Yet, the energy source term governing the latent heat release due to frost deposition was not included in the conservation equations, which could significantly affect the heat transfer process across the frost layer. Armengol et al. [28] suggested a frosting model by considering a two-dimensional growth rate. In their fixed grid and control volume-based approach, the generation of a secondary ice phase was achieved by calculating the diffusing vapor mass to a cell from the neighboring cells, due to concentration difference. The formulated model was validated over the experimental frost thickness data, showing a good agreement with altered environmental parameters. Wu et al. [29] derived a frost mass source term by incorporating the supersaturation level of the humid air. Their model validation was done by comparing the transient change of cold plate temperature during the frost deposition over it. Presented simulation results captured both lateral and vertical frost growth, in accordance with the experimental data. The presented model was also tested to calculate frosting inside and fin-tube heat exchangers [30]. The distortion of air flow between fin passages due to frosting was estimated. In the next research paper, Wu et al. [31] further improved the previously suggested mass transfer model. Their new model includes a phase change driving force, which was devised over Gibbs Free Energy. The numerical model was tested over a flat plate, and the validation of the model was performed over the experimentally measured frost thickness along with experimental frost mass measurement. The inclusion of the latter verification greatly increases the reliability of the proposed model. In a combined experimental and numerical study, Ma et al. [32] performed numerical analysis to model frosting over a wavy plate and validated their model with the experimental frost weight and thickness data. It was reported in the study that the propagating front of the growing frost layer over the plate was captured well compared to the empirical measurements, and this estimation enables the suitability of the proposed model to test various geometries. Kim et al. [33] formulated the mass source term by defining a frost formation resistance term. The model was able to capture both the densification and growth process of the frost layer. The model validation was done over the experimental frost thickness and density data obtained elsewhere. In another study, Lee et al. [21] developed their frosting model by considering the low surface temperature conditions and high frost porosity levels and improved the previous model [33]. An exponential term was included in the source term, to govern and limit the phase transfer. However, in both previously mentioned research [21,33], the latent heat generation was neglected, and not given to the computational domain. Furthermore, several studies focused on frosting model development under cryogenic conditions. Byun et al. [34] devised a phase transfer term based on supersaturation and dimensionless Stefan Number. A wide range of environmental conditions were considered in the simulations, and the developed model was compared against the experimental thickness and density data. Sun et al. [35] generated a frosting model and performed simulations under cryogenic conditions. In the developed mass source term, supersaturation and convective mass transfer coefficient were included. The effect of different mass transfer coefficient correlations on the frosting rate was examined. The comparison between the numerical model and experimental results was done over the temperature measurement across the channel. You et al. [36] applied a dynamic mesh technique to govern frost formation and growth. In their mass transfer model, the frosting source term was constituted as the function of local water vapor mass fraction. The model was run under different environmental conditions and obtained numerical results were compared with the experimental frost thickness. Local physical properties of the generated frost layer were estimated. In a more recent study, Xu et al. [37] put forward a mass transfer model considering the physical aspect of a frost layer. It was proposed in the model that the ice volume fraction of a cell must surpass a certain threshold, to ensure the stable growth of a frost layer. The model was verified with the gathered experimental frost thickness and density data from the literature. In the study, Wong et al. [38],], utilized a mass source term depending on convective mass transfer coefficient and supersaturation similar to Sun et al. [35]. Considering a very broad range of environmental conditions, they estimated the frost layer's thickness for each simulation. The validation of the model was also performed with frost thickness data, taken from literature. Overall, the previously developed and proposed frost modeling approaches over a source term implementation were summarized in Table 1.

There have also been other finite volume and Lattice Boltzmann based computational codes developed for frost modeling. Different from the Eulerian – Eulerian multiphase modeling, Bartons et al. [39] solved a single set of conservation equations for both phases in their fixed grid finite volume code. In the study, both solidification and sublimation phase changes were considered simultaneously, and phase transfer was generated with vapor mass flux balance. The validation of the computational code was done over the experimental frost thickness and frost mass data. In a different study, Negrelli et al. [40] developed a model combining a fractal theory and finite volume method. Based on the model, thermal conductivity of the frost layer was

Table 1: List of the previous numerical frost modeling studies performed with source term implementation.

Authors - Year	Considered Geometry	Modeling Methodology	The Proposed Mathematical Model is Based on	Data used for the Model Validation
Cui et al. [25]	Flat Plate	2D Numerical Modeling	Nucleation Theory	Experimental Frost Thickness
Cui et al. [26]	Fin and Tube Heat Exchanger	3D Numerical Modeling	Nucleation Theory	-
Kim et al. [27]	Flat Plate	2D Numerical Modeling	Water Vapor Mass Flux	Experimental Frost Thickness Theoretical Frost Density Theoretical Frost Surface Temperature
Armengol et al. [28]	Flat Plate	2D Numerical Modeling	Water Vapor Mass Flux	Experimental Frost Thickness
Wu et al. [29]	Flat Plate	2D Numerical Modeling	Water Vapor Supersaturation	Experimental Frost Mass Measurement Experimental Cold Plate Temperature
Wu et al. [30]	Fin and Tube Heat Exchanger	3D Numerical Modeling	Water Vapor Supersaturation	-
Wu et al. [31]	Fin and Tube Heat Exchanger	2D Numerical Modeling	Gibbs Free Energy	Experimental Frost Thickness Experimental Cold Plate Temperature
Ma et al. [32]	Wavy Plate	2D Numerical Modeling	Gibbs Free Energy	Experimental Frost Thickness Experimental Frost Mass
Kim et al. [33]	Flat Plate	2D Numerical Modeling	Frost Formation Resistance	Experimental Frost Thickness Experimental Frost Density
Kim et al. [21]	Flat Plate	2D Numerical Modeling	Frost Formation Resistance	Experimental Frost Thickness Experimental Frost Density
Byun et al. [34]	Flat Plate	2D Numerical Modeling	Gibbs Free Energy	Experimental Frost Thickness Experimental Frost Density
Sun et al. [35]	Flat Plate	2D Numerical Modeling	Water Vapor Supersaturation Convective Mass Transfer Coefficient	Temperature Measurement Across Channel
You et al. [36]	Flat Plate	2D Numerical Modeling	Water Vapor Mass Fraction	Experimental Frost Thickness Experimental Frost Density
Xu et al. [37]	Flat Plate	2D Numerical Modeling	Water Vapor Supersaturation	Experimental Frost Thickness Experimental Frost Density
Wong et al. [38]	Flat Plate	2D Numerical Modeling	Water Vapor Supersaturation Convective Mass Transfer Coefficient	Experimental Frost Thickness

calculated, by showing a good agreement against the acquired experimental data. A direct numerical simulation (DNS) analysis was performed by Zgheib et al. [41] for frost modeling. Immersed boundary method was implemented to govern frost growth at the interface. The validation study was performed over the frost thickness growth rate. In their next study, the developed code was tested under a range of environmental conditions [42]. Gong et al. [43] put forward a Lattice Boltzmann Model and simulated frost growth over a simple plate. Although the high resolution of the model well captured the dendric structure of the frost layer, the density seems to be overpredicted compared to previous experimental and numerical studies. It was found to be very close to density of ice across the frost layer. The validation of the code was done according to experimental frost thickness measurements, which could be the source of the overestimation in frost density.

In summary, knowing the heat transfer rates across a surface during a dynamic frosting process is important to know to assess the performance of the aforementioned thermal devices. However, despite the importance of knowing heat rates across a surface experiencing frost deposition, a very limited number of studies exist in the literature aiming to heat flux quantification. Therefore, the first objective of this thesis is to carry out a comprehensive experimental and numerical analysis to investigate dynamic heat flow across a growing frost layer under various forced convection conditions. Concerning the modeling side, the validations of previously referenced numerical models vastly depend on the experimental frost thickness data. However, frost thickness data or theoretically obtained density calculations could be greatly misleading for validation purposes. Thermal properties of the frost layer, such as density and thermal conductivity, might exhibit great independence to frost height. Thus, heat flow across a frost layer is a more reliable indicator of a frost structure, such that both porosity and frost thermal conductivity could be more accurately estimated. Notwithstanding the extensive number of CFD studies, especially the ones that use source term driven frost modeling, there still exists a lack of reliable validation analysis for most of the established models. Thus, in this thesis, a high accuracy frost model is aimed to be developed based on empirical data.

This thesis is composed of five chapters. The first chapter was dedicated to provide an insight into frost formation, referring to some of the significant studies focusing on frost modeling and experimental analysis. In the second chapter, details of the utilized system to perform frosting experiments are explained. In the third chapter, an Euler – Euler based numerical model development to simulate frosting conditions is explained. In the next chapter, the obtained experimental results are discussed in detail. In the fifth chapter, the application of developed numerical model and simulation results are shown. The next chapter highlights the main conclusions drawn from the study, and finally in the last chapter some of the future works are recommended by the author.

CHAPTER II

EXPERIMENTAL SYSTEM

In this chapter, the utilized experimental system and employed techniques are shown in detail. The measurement methodology of heat transfer rate during frosting process is explained.

2.1 Experimental Apparatus

An experimental system is designed and built for the current research. Figure 3 shows the experimental system. The system consists of an air conditioning chamber, frosting test section, heat flux measurement system, sensors, and data collector devices. The system was well insulated except the test section, to eliminate any heat exchange with the surrounding. The ambient conditions of the test rig were controlled by means of air conditioning chamber. It consists of a chiller and a humidifier. The chamber was mounted to the system to control air temperature and relative humidity levels. A thermostatic bath was used to control air temperature, where a working fluid was circulated through the evaporator coils that were fixed inside of this chamber. Humidity control was achieved by using a physical programmable circuit board, in which data acquired from humidity the sensors was transferred. Two Omega USB enabled temperature and humidity sensors with a custom data acquisition software are used to monitor the temperature and humidity data continuously, and they held constant during the experiments with variations of ±0.2°C and ±0.5 % respectively. Experiments were conducted inside of the frosting test section, having a cross sectional area of 130 x 130 mm^2. The length is 50 cm, with a contraction and expansion sections at the inlet and outlet. Test section consists of a flow straightener with 400 subchannels each with a length to diameter ratio of 8, a heat flux measurement

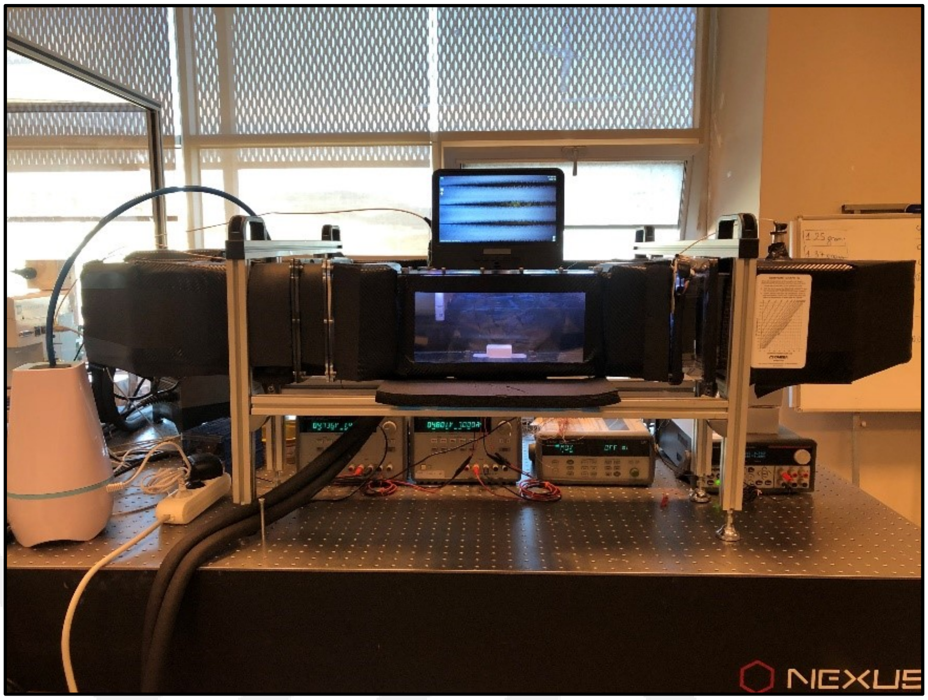

Figure 3: Experimental Setup

system, and a fan which can vary the air velocity in the range of 0 to 2 m/s by means of a power supply. Humidity and temperature sensors positioned at directly above the test plate and downstream of it. A fan was positioned at downstream of the test section, such that suction type of air flow was ensured. CEM DT-8880 hot wire probe was used to monitor the air velocity. The test section was made of plexiglass to have visual access. The frosting process was continuously recorded by using a Phantom V311 high-speed camera. The thickness of the frost layer was derived by post-processing the recorded frost images in MATLAB Image Processing Toolbox. Regarding the image resolution, 1 mm length was captured by 13 pixels .

The general layout of the setup is depicted in Figure 4.

2.2 Heat Flux Measurement System

The layout of the heat flux measurement system is shown in Figure 5. The test surface was cooled using 2 thermoelectric devices (TEC) positioned at the bottom.

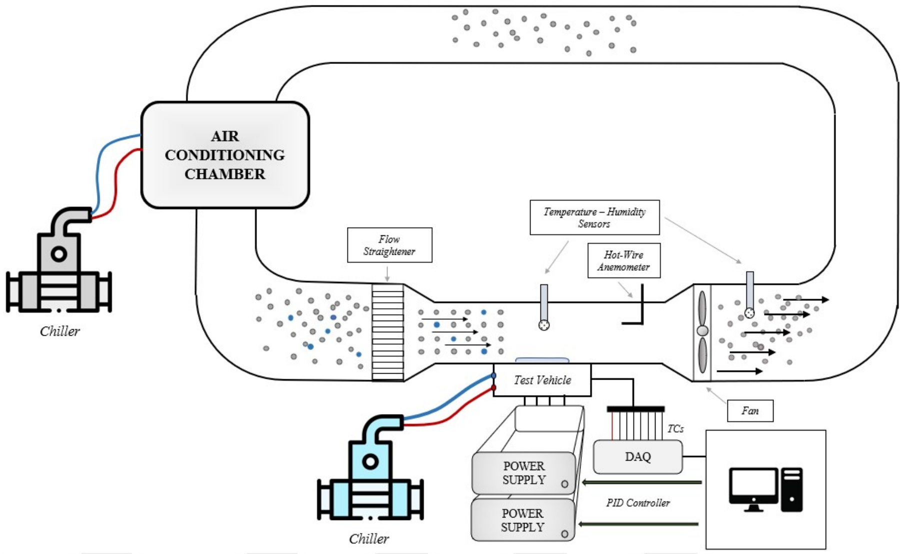

Figure 4: Illustration of the experimental facility

The hot sides of the TECs were attached to a cold plate, which was made by aluminum. It was cooled by another chiller, through which generated heat rejected by the TEC devices was absorbed. Temperatures of the TECs were controlled by a PID controller algorithm such that temperature uniformity over the frosted surface was ensured within an accuracy of ±0.5°C. The temperature of the frosted test surface was measured using four T-type thermocouples with a diameter of 0.64 mm, which were mounted directly below the frosted surface. Thermocouple probes were uniformly distributed below the test surface at four different locations. To ensure flatness of the frosted surface without any buckling, channels were drilled to the measurement surface as a bed for thermocouple probes. A 1 mm thick steel plate with dimension of 40x80 mm^2 was utilized as the test surface for frost deposition. A thermal paste with a thermal conductivity of 11 W/m-K was applied between the measurement plate and test surface to minimize the contact resistance. Due to the negligible thermal resistance of the steel plate, thermocouple temperature readings correspond to the temperature of the frosting surface. Thermocouple and TEC wires were connected to the data acquisition device from under the bottom of the test section. Between the measurement plate and test surface, a thin film heat flux sensor with a thermal

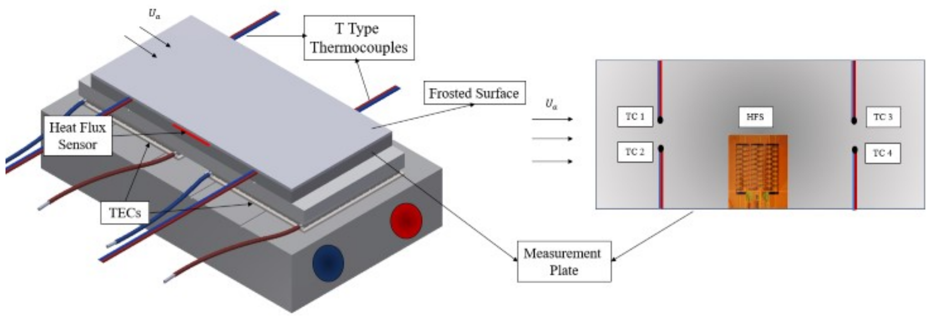

Figure 5: Details of the test vehicle

resistance of 0.00176 mm^2-K/W (Omega HFS-3) was placed to monitor the transient changes in the heat flux during the frost deposition on the surface. Same as thermocouple beds, measurement surface was machined to place heat flux sensor to provide flatness. The system was insulated from the sides with specifically manufactured 3D printed casing. The heat flux measurement system was inserted to the test section, and only test surface is exposed to the air flow.

2.3 Test Procedure

Before each experiment, the top of the surface was cleaned and covered with an aluminum foil to get rid of initial frost transients until the system reaches a steady state. This way, the accumulated frost layer on the plate during the initial cooling period was taken out from the test surface. The frosting process could exactly be initiated at the desired temperature conditions without a presence of frost layer over it. Later, the foil was removed by operator, through the access located above of test section, without inducing any disturbance to ambient conditions. After removing the foil, the real frosting process started above the test plate, and dynamic heat transfer measurements were taken.

Table 2 presents the list of the experiments conducted in this study. A total of fifteen experiments were carried out to investigate the effects of different air velocities and frosted surface temperatures on frost formation and heat transfer rates.

Table 2: List of experiments

Case No	Air Velocity [m/s]	Air Relative Humidity[%]	Cold Plate Temperature [°C]	Air Temperature [°C]
C-1	1.0	50	-6	25
C-2	1.0	50	-10	25
C-3	1.0	50	-20	25
C-4	1.0	50	-30	25
C-5	1.5	50	-6	25
C-6	1.5	50	-10	25
C-7	1.5	50	-20	25
C-8	1.5	50	-30	25
C-9	2.0	50	-6	25
C-10	2.0	50	-10	25
C-11	2.0	50	-20	25
C-12	2.0	50	-30	25
C-13	2.0	50 to 73	-30	25
C-14	1.0	50	-10	25
C-15	1.0	50	-30	25

Initially, twelve experiments were carried out under three different air velocities and four different frosted surface temperatures. Next, an experiment was done with an instantaneous increase in the air relative humidity from 50 % to 73 %, for further quantification of latent heat flux. The last two experiments were carried out to analyze frost growth in very low air velocities, which is close to the natural convection conditions.

2.4 Uncertainty Analysis

Uncertainties are inevitable in experimental measurements. In this study, major sources of uncertainties stems from system errors (Bias) and Random (Precision). They both constitute the total error. Accordingly, uncertainty analysis was carried out to find the total error, within a 95 % confidence bound [44].

The bias errors are associated with the accuracy (A) and resolution (R) of the utilized sensors with the formula:

Table 3: Experimental uncertainties

Measured Variable	Measured range	Bias Error	Precision Error	Total Uncertainty	Relative Uncertainty [%]
u_a	0.7 to 2.0	0.11	$4.2x10^{-4}$	±0.1	6.6
T_a	25	1.001	-10	±1	4.1
$\phi[\%]$	50	3.001	0.02	±3	6.1
$T_s[^\circ C]$	-6 to -30	1.001	0.002	±1	4.0
$\delta[mm]$	0 to 4	0.067	-	±0.067	3.3
$q"[W/m^2]$	500 to 1500	5.000	0.0847	±5	0.5

$$B_x = [(0.5R)^2 + A^2]^{0.5} \tag{1}$$

Precision error is related to the mean standard deviation of the acquired data during the experiments. The calculation could be made with the following equation:

$$P_x = t_{(n-1),95\,\%}\sigma_{\overline{x}} \tag{2}$$

Then, the total uncertainty was calculated via Eq. (3) :

$$T_x = [{B_x}^2 + {P_x}^2]^{0.5} \tag{3}$$

Table 3 shows the measured quantities and their total and relative uncertainties. The measurement ranges of each parameter were also given. To determine relative uncertainty, an average value was chosen among the measurement range of each parameter.

CHAPTER III

NUMERICAL MODEL

This chapter explains the followed numerical methodology to model frosting process. An in house developed computational code governing the frosting mechanism is implemented to a commercial CFD solver.

3.1 Governing Equations

Frosting is a phase change process during which gaseous water vapor transforms into solid ice. Accordingly, in this thesis study, Euler-Euler type multiphase modeling approach was followed to model the two phases, namely solid ice and gaseous water vapor. In this approach, the conservation equations are solved for each phase individually, and both phases are considered as continuous. To determine the phase volume fraction for each phase, a volume fraction equation was solved, which is given in the Eq. (4):

$$\frac{\partial \alpha_i}{\partial t} + \nabla(\alpha_i V_i) = 0 \tag{4}$$

The sum of volume fractions of these phases is equal to 1, within each computational cell.

$$\alpha_i + \alpha_{ha} = 0 \tag{5}$$

The conservation equations of continuity, momentum and energy equations were solved for each corresponding phase. These are given below respectively.

$$\frac{\partial \alpha_q \rho_q}{\partial t} + \nabla(\alpha_q \rho_q V_q) = S_M \tag{6}$$

$$\frac{\partial \alpha_q \rho_q V_q}{\partial t} + \nabla(\alpha_q \rho_q V_q V_q) = K_{iq}(V_p - V_q) - \alpha_q \nabla_p + \nabla \bar{\bar{\tau}}_q + S_q \tag{7}$$

$$\frac{\partial \alpha_q \rho_q h_q}{\partial t} + \nabla(\alpha_q \rho_q V_q h_q) = -\nabla q_q + \alpha_q \frac{\partial P_q}{\partial t} + \bar{\bar{\tau}}_q : \nabla V_q + S_h \tag{8}$$

In the current multiphase model, humid air phase was composed of water vapor and dry air. Then, a separate species transport equation was solved for the water vapor component of the humid air phase.

$$\frac{\partial \alpha_{ha} \rho_{ha} w_{va}}{\partial t} + \nabla(\alpha_{ha} \rho_{ha} V_{ha} w_{ha}) = \nabla(\rho_{ha} D_{H_2O} \nabla w_{va}) + S_{va} \tag{9}$$

In Eq. (9), the first term on the right-hand side governs the water vapor diffusion, and D is being the diffusion coefficient. The considered assumptions and simplifications done in the current model are listed in below:

- The proposed model considers only water vapor deposition, considering the low temperature to surpass condensation dominated frosting mechanism.
- Sublimation of ice is neglected.
- Gravitational effects are not included.
- Water vapor diffusion coefficient is considered as constant.
- Turbulent effects are not included.

3.2 Frost Mass Accumulation Model

The mass transfer between the phases could be accomplished by using source terms appearing in the continuity equations. In this regard, many different source term driven frosting models have been proposed in the literature [21, 25–38], following general form given in Eq. (10) as:

$$\dot{m} = \tau(\rho_{ha}\alpha_{ha})(w_c - w_{sat}) \tag{10}$$

In this equation, the excess humidity content in air is considered as the driving potential for frosting. However, the presence of the excess humidity may not always lead to frost accumulation. The rate of the frost accumulation also depends on other factors as described by the crystal growth theory. Known as the attachment kinetics, the incorporation of water molecules to an ice lattice is one of the parameters affecting the frosting rates. Generally, attachment kinetics can be very complex, micro-level, and depend on various factors such as surface chemistry, lattice structure etc. Along with the attachment kinetics, water vapor diffusion across a frost layer is another factor controlling the amount of deposition. The path that a water vapor molecule travels within a porous frost layer is affected by ice crystal types and this could limit the frosting rate. The further detailed explanation about both kinetic and diffusion limited growths could be found in the Libbrecht's study [45]. In Eulerian-Eulerian modeling approach the effect of those factors can be expressed with a single parameter τ which can be tuned using the available experimental data. The methodology that was used in the present study in the evaluation of τ is discussed in the Section 5.

In addition to that, frost deposition on surface also depends on the velocity field inside the thermal boundary layer formed on the cold surface. Experimental results show that even though conditions that favor frost accumulation exist in a large portion of the thermal and concentration boundary layers, frost formation is only observed over the existing frost layer on the cold surface. This behavior implies the need for a velocity dependent parameter κ in the calculation of the frost mass source term. So, the final form of the frost mass source term used in this study is given in Eq. (11). The detailed tuning process of the proposed parameter κ is also discussed in the Section 5.

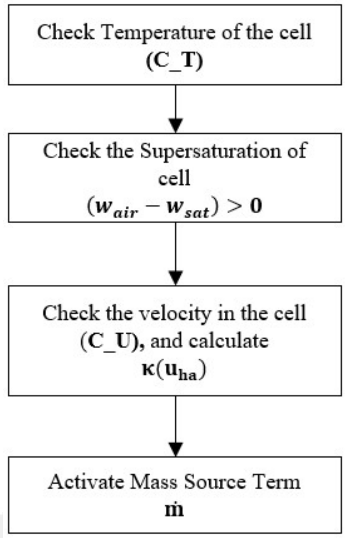

Figure 6: Algorithm for frost modeling

$$\dot{m} = \tau\kappa(\rho_{ha}\alpha_{ha})(w_c - w_{sat}) \tag{11}$$

Similar to the previous studies, water vapor supersaturation was included in the model as a main driving force of the phase change. It represents the excess amount of humidity which is ready for deposition. The last term appearing in Eq. (11) is the water vapor mass fraction at the saturation humidity level, $w_{sat}(T_{ha})$. It is linked to temperature, and calculated according to the correlation of saturation partial pressure of water vapor over ice [46].

The developed mass source term was employed in the cells according to the flowchart given in Figure 6. First and foremost, temperature of a humid air phase cell is monitored, and the condition of being below the freezing point of the water is checked. Next, the existence of supersaturation in the cell is verified. If these two conditions hold, the value of $\kappa(u_{ha})$ is determined to cover the accumulation time. According to this procedure, the amount of phase transfer $\dot{m}$ is calculated and inputted to the frost phase cells.

3.3 Interaction Between the Phases and Source Terms

In the Eulerian approach the interface between the phases is not resolved. This requires a separate heat transfer model for the calculation of heat transfer between the phases. For the modeling of the heat transfer between the phases the Nu correlation given in Eq. (12) is used [47]

$$Nu_q = 2.0 + 0.6{Re_q}^{0.5} Pr^{0.33} \tag{12}$$

Here, Re_q is the relative Re and calculated according to the secondary phase diameter and relative velocity $|V_i - V_{ha}|$ between the two phases. In the Eulerian modeling approach, the secondary phase, the ice, is considered as small spherical particles. In this study, the diameter of the ice phase was set to 10^{-5} m.

To model the drag force exerted by humid air phase to ice phase, Schiller and Neumann model [48] was used to determine the drag coefficient between the phases, which is given in below:

$$f = \frac{C_D Re}{24} \tag{13}$$

where,

$$C_D = \begin{cases} \frac{24(1+15Re^{0.687})}{Re}, & Re \leq 1000 \\ 0.44, & Re > 1000 \end{cases} \tag{14}$$

As it was mentioned before, the mass transfer between the phases was generated over the source terms, based on the model given in the Eq. (11). Table 4 summarizes the added source and sink terms to the conservation equations.

In the Table 4, h_{sub} represents the latent heat release due to the water vapor deposition. In this model, its value was calculated separately for each cell using the Clausius – Clapeyron equation [49], which was given in the Eq. (15)

Table 4: Source Terms

Source term	Humid air	Frost
S_m	$-\dot{m}$	$\dot{m}$
S_q	$-\dot{m}V$	$\dot{m}V$
S_h	$\dot{m}h_{sub}$	-
S_{va}	$-\dot{m}$	-

$$\ln\left(\frac{P_c}{P_{ref}}\right) = \frac{h_{sub}}{R_{va}}\left(\frac{1}{T_{ref}} - \frac{1}{T_{ha}}\right) \tag{15}$$

Where P_{ref} and T_{ref} represents the water vapor reference states of 3.988 kPa and 298.15K, respectively. So, the sublimation enthalpy could be calculated for any other state and each cell in which frosting occurs at vapor pressure, P_{cell}, and temperature, T_{ha}.

3.4 Computational Domain, Boundary and Initial Conditions

The conservation equations listed above are subjected to boundary conditions. Figure 7 shows the computational domain and the boundaries. The domain was considered as two-dimensional, and simulations were performed in transient. Overall, the boundary conditions were given as follows:

(1) Left: Velocity inlet boundary condition

$u_{ha} = u_{in}$, $v_{ha} = 0$, $T_{ha} = T_{in}$, $\alpha_{ha} = 1$, $\alpha_i = 0$, $w_{va} = w_{in}$, $w_{da} = 1 - w_{in}$.

(2) Right: Pressure outlet boundary condition

The gauge (static) pressure at the outlet was set to zero.

$P_{st} = 0$.

(3) Top and bottom walls (Except the cold wall): Adiabatic and no slip condition

$u_{ha} = v_{ha} = 0$, $u_i = v_i = 0$, $\frac{\partial T_{ha}}{\partial y} = \frac{\partial T_i}{\partial y} = 0$, $\frac{\partial w_{va}}{\partial y} = 0$.

(4) Cold wall: Fixed temperature and no slip

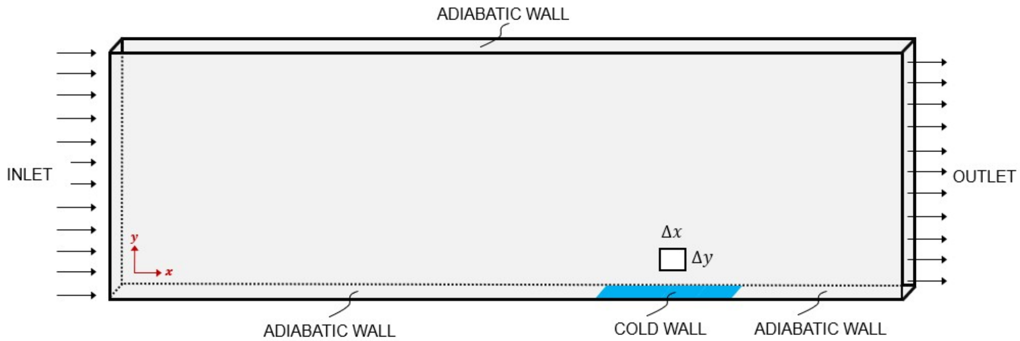

Figure 7: Sketch of the 2D computational domain

$u_{ha} = v_{ha} = 0$, $u_i = v_i = 0$, $T_w = T_{set}$ $\frac{\partial w_{va}}{\partial y} = 0$, $\frac{\partial \alpha_i}{\partial y} = 0$.

The temperature of humid air phase and water vapor mass fraction were given as initial conditions as 298 K and 10.256 g/kg respectively. In the entire domain, the ice phase motion was restricted, and its velocity was set to zero.

3.5 Solution Methods and Grid Sensitivity Analysis

A pressure-based solver was used in the calculations. The SIMPLE algorithm was employed to couple velocity and pressure. The volume fraction equation was discretized by using 1st order linear upwind scheme. Mass, momentum, and energy equations were discretized with 2^{nd} order linear upwind discretization scheme. Transient terms in the conservation equations were handled by using 2^{nd} order Implicit method. Furthermore, the source terms were discretized implicitly by applying Picard's approximation method. In this method, the derivatives of the source terms were provided to enhance solution stability. Therefore, higher time step sizes could be achievable without experiencing stability issue. Accordingly, source terms were written as the following form:

$$S_\phi = G + H\phi \tag{16}$$

where,

Table 5: Independent Variables for the source term linearization

Equation	Independent Variable ϕ	
	Humid Air	Ice
Volume Fraction	α_{ha}	α_i
Momentum	$\vec{V}_{ha}$	$\vec{V}_i$
Energy	h_{ha}	-
Species Transport	w_{va}	$-$

$$G = S(\phi) - \left.\frac{\partial S}{\partial \phi}\right|_{\phi_0} \phi_0 \tag{17}$$

$$H = \left.\frac{\partial S}{\partial \phi}\right|_{\phi_0} \tag{18}$$

where ϕ is independent variable, and ϕ_0 is the expansion point. Accordingly, all source terms considered in the 4 were implicitly treated by supplying their derivatives with respect to ϕ. The independent variables for each conservation equation and corresponding phase were given in Table 5.

To decide the time step size, unsteady simulations were carried out by considering different time step sizes of 0.5, 1.0 and 2.0 and 5.0 seconds. It was observed that the calculated heat flux exhibits no big difference for time steps less than 1.0 s. Hence, all numerical simulations were performed with this selected time step size. Furthermore, a grid sensitivity analysis was also carried out before conducting the frosting simulations. Throughout the domain, a structured hexahedral type of mesh was used. The sensitivity analysis was conducted by considering the average heat transfer coefficient over the cold wall. 5 different δ y distances were evaluated, and results were plotted in the Figure 8. The average heat transfer coefficient becomes insensitive to further mesh refinement below 400 x 400 μm grid resolution. Although this grid level is found to be reliable for the simulations, the mesh size of 100 x 100

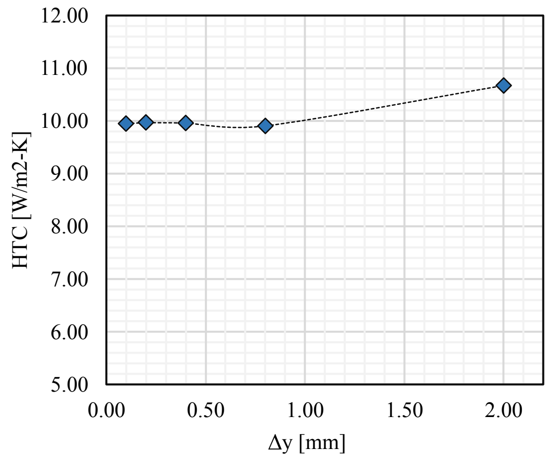

Figure 8: Grid sensitivity analysis with respect to convective heat transfer coefficient.

μm was determined to use in the cold plate vicinity. So that, increase in the frost layer thickness and gradients could be tracked with a greater resolution by using this cell size.

CHAPTER IV

EXPERIMENTAL RESULTS

In this chapter, results of the experiments are shown in detail. A mathematical analysis over the collected heat transfer and frost thickness data is conducted to characterize the frost layer.

4.1 Preliminary Mathematical Analysis

When an energy balance is applied over the frost surface, total heat flux through the sensor can be calculated as:

$$q''_{total} = Lh_{mass}(w_{air} - w_{fs}) + h_{air}(T_{air} - T_{fs}) \tag{19}$$

According to Eq. (19), total heat flux was decomposed into two parts. The first term on the right-hand side stands for the latent heat release due to the total mass coming to frost surface from air. The second term is attributed to the sensible heat part driven by the temperature difference between air and the frost surface. Radiative heat transfer was neglected, due to small temperature differences between the frost surface and surroundings [10, 15, 18]. Convective heat and mass transfer coefficients can be linked to each other with Chilton-Colburn analogy as:

$$h_{air} = h_{mass} c_p Le^{\frac{2}{3}} \tag{20}$$

A number of studies [11, 19, 23] have shown that Lewis number is very close to 1 based on experimental measurements. Therefore, it was accepted as 1 in this study. To determine the heat transfer coefficient, h_{air}, measurements were conducted on the flat plate at dry conditions in the absence of frosting for three different air velocities.

Table 6: Convective Transfer Coefficients

Air Velocity $[m/s]$	$h_{air}[W/m^2-K]$	$h_{mass}[W/m^2-s]$
1.0	10.4	0.0104
1.5	12.6	0.0126
2.0	14.5	0.0142

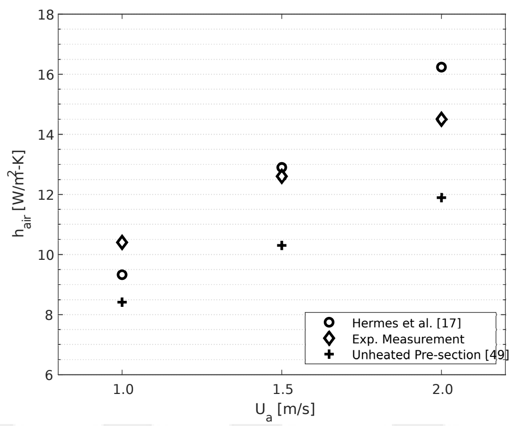

Figure 9: Measurement of convective heat transfer coefficient and comparison with literature.

Accordingly, measured, and calculated values of h_{air} and h_{mass} were given in Table 6. Figure 9 also shows the comparison of the measured heat transfer coefficient with the correlations from literature.

4.2 Evaluation of Frost Thickness and Heat Flux During Frosting

Figure 10 illustrates the complete frost thickness data measured for all cases. Overall, at different test conditions covering four different surface temperatures and three different air velocities, frost thickness showed a continuous rise over the course of the process. Especially at low surface temperatures initially a steep rise in the frost thickness was observed which rapidly slows down with increasing frost thickness. On the other hand, a stable frost thickness increase was observed at higher cold surface temperatures. The considerable differences in the frost thicknesses between

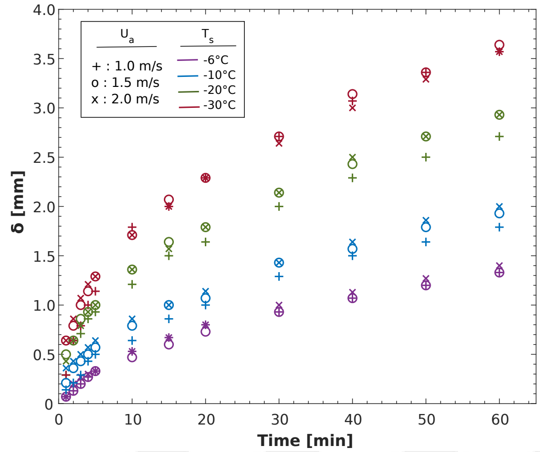

Figure 10: Variation of frost thickness over time for a range of air velocities and temperatures.

the different cold surface temperatures at the end of the measurement duration are mostly due to the difference in the frost growth rates at the early stages of frosting. Figure 10 shows that, within the first 10 minutes of frosting, the rate of increase in the frost thickness is the highest for the cold plate temperature of −30℃, with 0.17 mm/min. This rate was calculated as 0.06 mm/min and 0.08 mm/min for the plate surface temperatures −6℃ and −10℃ respectively. Accordingly, it is deduced that the speed of frost front propagation is majorly governed by the frost surface temperature, which is greatly affected by the cold plate temperature. Regarding the effect of the air velocity on the frost growth rate one can say that the final frost thicknesses are quite similar at different air velocities. The effect of air velocity on frost thickness growth was also discussed in [17, 19] and similarly, no major effect of the air velocity on frost thickness growth was found as well. The maximum difference was found as 0.21 mm between Case 6 and Case 10.

A similar trend with the frost thickness is also found with the heat flux. Figure 11 shows the measured heat flux and frost thickness levels over time. Overall, heat flux showed a continuous decrease during frosting. Moreover, the rate of decrease in the heat flux is not constant over time but shows a decreasing trend. The physical mechanism that leads to the observed behavior in the heat flux could be better analyzed by deriving the time derivative of the heat flux as:

$$\frac{dq''}{dt} = -(T_{air} - T_s)\frac{dR_{tot}(t)}{dt}\frac{1}{R_{tot}^2} \tag{21}$$

Here, R_{tot} refers to the total heat transfer resistance between the cold surface and the incoming air. Due to the developing frost layer over time, the total resistance is also a function of time. According to Eq. (21), the rate of change in the heat flux is proportional to the rate of change in the overall thermal resistance. The rate of change in the overall resistance is a function of frost thickness. As shown in the measurement results, the rate of increase in the frost thickness is decreasing over time which is expected to result in a decrease in the rate of increase in the total resistance. However, there is a second effect that affects the rate of change in the heat flux level. As shown in Eq. (21) the time rate of change in the total resistance is scaled with the square of the total thermal resistance at that time. Accordingly, even if the rate of change in the total resistance were constant, the rate of change of the heat flux would still have decreased over time due to the increase in the total resistance term in the denominator.

In Eq. 12, total heat flux drops at the end of the experiments were illustrated on a percentage scale. The first readout of the heat flux sensor was accepted as initial heat flux, and percentage ratios were calculated based on that value. Accordingly, the most significant drop in the heat transfer was found to take place within the first 20 minutes nearly for each case, which is one third of the total experimental duration. It was seen that, as the cold plate gets cooler, the heat flux drop becomes more significant. When the percentage drops between the surface temperatures of −30°C and −10°C are compared with each other, one can notice that for each respective air velocity; decreases in heat transfer after 20 minutes were more abundant for −30°C.

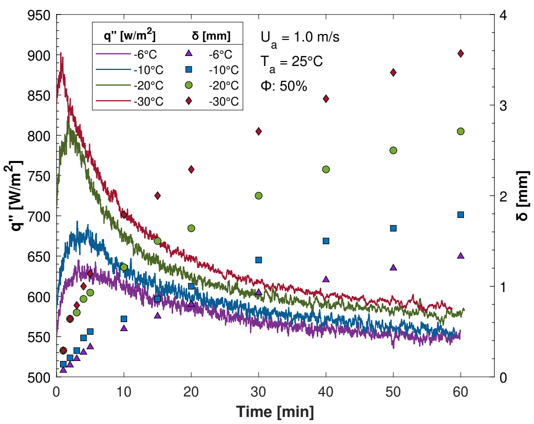

(a)

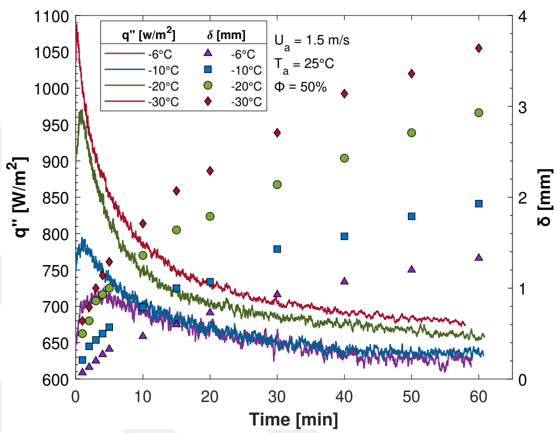

(b)

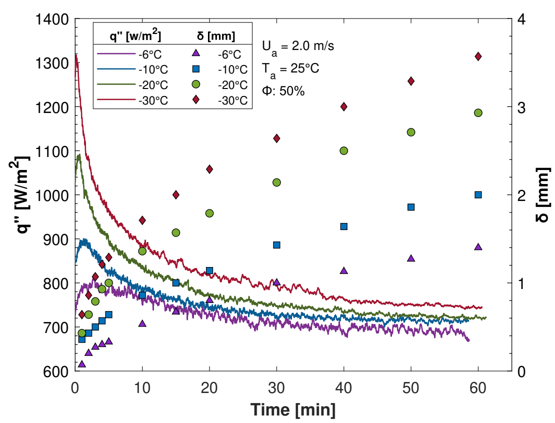

(c)

Figure 11: Heat flux curves and frost thickness belonging to Case 1 to 12.

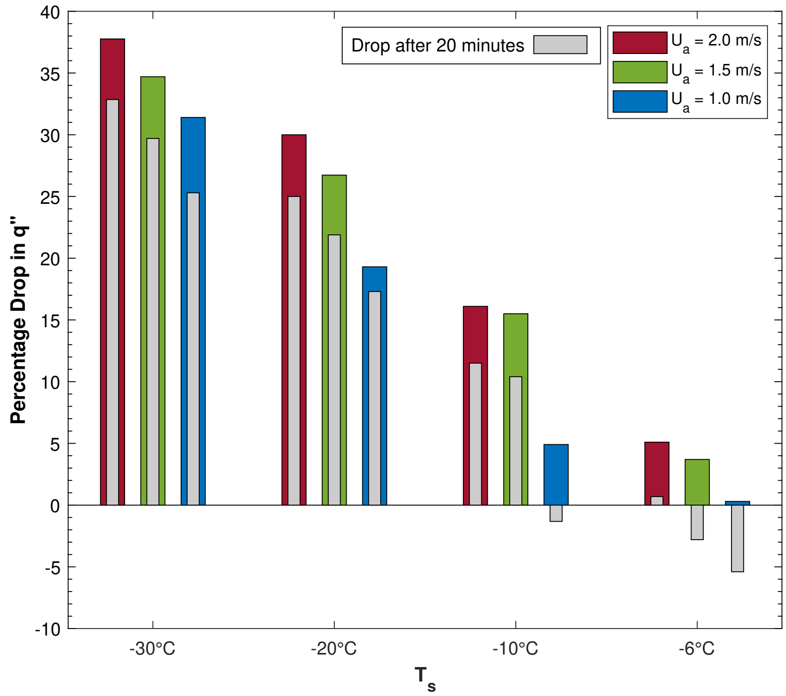

Figure 12: Percentage decreases in the Total Heat Flux.

For example, for the Case 12, 33% percent of total heat flux drop (38%), was already observed after 20 minutes. For the Case 10, total heat flux drop was denoted as 16% at the end of experiment, while 11% drop was occurred after 20 minutes. Additionally, for Cases 1, 2 and 5, expected drop in the heat transfer seems to be recovered by the initial rise in the heat transfer, which will be discussed in the next section.

4.3 Heat Transfer During the Rapid Growth Phase of Frost

In the previous section, the decrease in the heat flux during the frosting process was discussed. The drop in the heat flux is due to the increase in the thermal resistance with the growth in the frost layer. However, as shown in Figure 12, under certain experimental conditions, a rise in the heat flux was measured at the initial stage of frosting and after reaching to a maximum the heat flux starts to decrease. Especially in the test conditions where the air velocity is low and cold surface temperature is high, a clear rise in the measured heat flux level was observed. For instance, the most prolonged rise was seen in the case when the surface temperature and air velocity are at −6°C and 1.0 m/s, respectively. On the other hand, when the air velocity and surface temperature are at 2.0 m/s and −30°C respectively, the heat flux curve showed a steep drop without any observable rise in the heat flux. The increase in the heat flux can be attributed to two sources. The first source is due to formation of extra heat transfer surface area, which is caused by the growing frost layer itself. Condensed water droplets over the cold plate and induced fin shaped ice crystals stemming from those nucleates might significantly promote the available surface area for heat transfer. The second source might be the possible increase in the convective heat transfer coefficient over the frost surface during the ice crystal growth process due to the increase in the surface roughness during initial frost accumulation. Yun et al. [10] conducted measurements on the heat transfer coefficient over the frost surface during the frosting process. Their results revealed that, the rough profile of the frost layer led to a rise of 60% in the heat transfer coefficient in the early stage of frosting.

To further investigate these two factors, two additional experiments were conducted at the air velocity of 0.7 m/s and compared with the heat flux behavior at 2.0 m/s, and experimental results are shown in Figure 13. Accordingly, at the air velocity of 0.7 m/s approximately 14% rise in the heat flux was measured at the surface temperature of −30°C. On the other hand, no heat flux rise was measured at the air velocity of 2.0 m/s. Furthermore, at the surface temperature of −10°C an even more prolonged heat transfer rise was observed at the air velocity of 0.7 m/s.

Figure 14 compares the frost layers at 0.7 m/s and at 2.0 m/s for the same cold surface temperature of –30°C. At 0.7 m/s a spikier frost layer is seen compared to the frost layer formed at 2.0 m/s. The relatively low humidity transport into the growing frost layer at 0.7 m/s might result in a more favorable frost growth in vertical direction rather than in lateral direction resulting in a spikier frost shape at the surface. These fin–like structures might have caused the increase in the heat flux at the initial stages

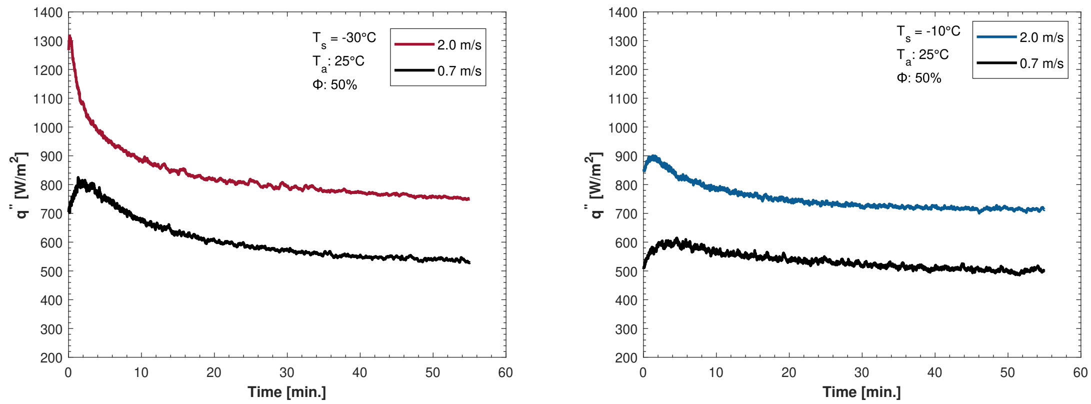

(a) (b)

Figure 13: Comparison of initial heat flux rise for $T_s = -10°\text{C}$ and $-30°\text{C}$, when air velocity is decreased down to 0.7 m/s.

of the frosting. However, at 2.0 m/s the enhanced humidity transport rate into the frost might have accelerated the growth of the frost in lateral directions as well which results in a more uniform frost surface. The difference in the mass transport rates due to the change in the air velocity might have resulted in the observed differences in the frost layers and in the heat flux behaviors. Similarly, a heat transfer rise during the early stage of frosting was also reported in the study conducted by Tahayyor et. al. [50]. Different from the current study, in that research frost was formed under natural convection conditions, and over a cylinder which has a considerably bigger surface area than the cold plate used in this research. According to their measurements, a 9% rise was denoted after 25 min, in the environmental conditions very similar to Case 14.

4.4 Individual Contributions of Sensible Heat and Latent Heat

Total heat flux into the surface is due to both sensible and latent heats. The sensible heat into the surface is driven by the convective heat transfer coefficient, h_{air} , and the latent heat is driven by the convective mass transfer coefficient, h_{mass} . These two

Figure 14: Visual comparison of ice crystal growth when between different air velocities where T_s= −30°C , T_a = 25°C , RH= 50% (a) Longer and spiky frost structure at 0.7 m/s (b) More uniform frost growth at 2.0 m/s.

coefficients could be related to each other with the Chilton-Colburn Analogy Eq. (20). Using this analogy, the contribution of the latent and sensible heat flux to the total heat flux to the surface could be derived. However, the validity of this approach could be tested by instantaneously increasing the humidity level and measuring the rise in the heat flux. In this regard, air relative humidity level was instantaneously increased from 50% to 73% and kept constant at that level for approximately 5 minutes. Figure 15 shows a 171 W/m^2 increase in the total heat flux as a result of the rise in the humidity level. Since the air temperature was kept fixed, no change in the sensible heat transfer is expected but the increase in the heat flux must have been entirely due to the increase in latent heat transfer. Next, the increase in the latent heat flux is calculated as:

$$q''_{lat} = Lh_{mass}(w_{air} - w_{fs}) \tag{22}$$

The calculation shows a 180 W/m^2 increase in the latent heat flux. The difference between the experimentally measured rise in the latent heat flux and the rise calculated using the Chilton-Colburn analogy is within the measurement uncertainty (95%). After experimentally validating the approach for relating the latent and sensible heat transfer contributions, the individual contributions of sensible heat and latent heat fluxes to the total heat flux could be analyzed for different experimental conditions.

Figure 16 shows sensible and latent heat fluxes for Cases 10 and 12. In both cases the heat flux due to the sensible heat transfer was found to be higher than the latent heat transfer at 50% relative humidity level. However, over time with increasing frost thickness the sensible heat flux showed a more pronounced drop in comparison to the latent heat. The higher sensitivity of the sensible heat flux to the frost thickness is due to the fact that the sensible heat transfer is directly proportional to the temperature difference between the frost surface and the air. On the other

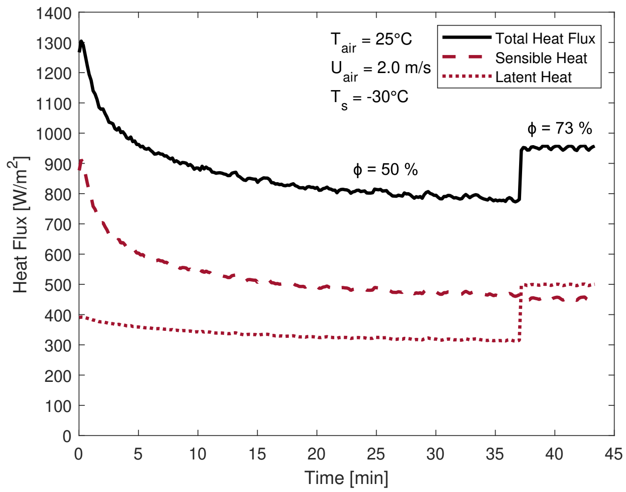

Figure 15: Variation of total heat flux with respect to a change in the latent heat flux. Red lines indicate the calculated heat flux values, and the black line is the experimental measurement.

hand, latent heat transfer is driven by the difference in the water vapor equilibrium concentration levels ($w_{air} - w_{fs}$) which is also a function of temperature. However, due to the nonlinear behavior of the equilibrium humidity level with respect to the temperature, latent heat transfer is much less sensitive to the changes in the frost surface temperature [7, 9].

4.5 Frost Surface Temperature

Measuring the frost surface temperature accurately is challenging due to the large temperature gradients across the thickness of the frost. However, the frost surface temperature could be derived from the heat flux measurement data. Many of the previous studies [11, 23] assumed saturated conditions on the air-frost surface interface. Based on this assumption, one can relate the measured heat flux with the frost surface temperature [19], T_{fs} , by using Eq. (23):

$$q''_{total} = Lh_{mass}(w_{air} - f(T_{fs})) + h_{air}(T_{air} - T_{fs}) \tag{23}$$

Figure 17 shows the estimated frost surface temperatures during the experiments.

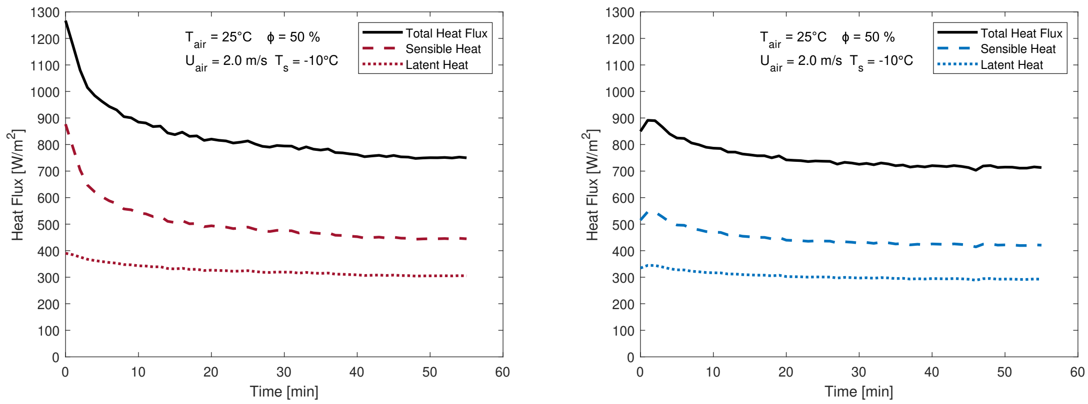

(a) (b)

Figure 16: Variation of total heat flux in terms of sensible and latent heat.

According to the results, initially when there is no frost layer on the plate the frost surface temperature is equal to the plate temperature. However, with time the frost surface temperature rises due to the growing thermal resistance between the cold plate surface and the air. After about 20 min, the differences between the frost surface temperatures drop down to less than 5°C. Results also show that there is an increase in the surface temperature rise with increasing air velocity. Similar observations were also presented in [9].

4.6 Effect of Densification to Frost Thermal Resistance

Thermal properties of the frost change during the course of the frosting process. As the frost layer grows into the flow, the frost surface temperature increases which alters the porosity and thermal conductivity of the top frost layer. Moreover, the thermal characteristics of the frost layers below the frost surface also continuously change due to the densification process. The difference in the equilibrium water vapor concentration levels drives the mass transfer into the inner frost layers, increasing the density and thermal conductivity of the inner frost layers over time. To analyze the effect of the densification process on the overall thermal resistance of the frost layer, the total conduction resistance of the frost layer is expressed as in a two-layer

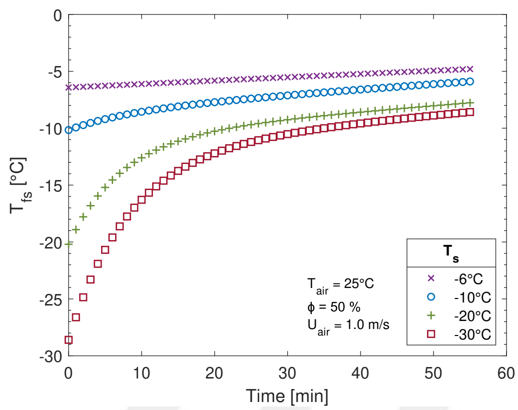

(a)

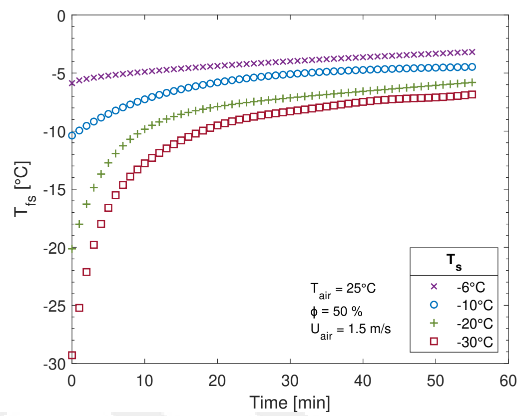

(b)

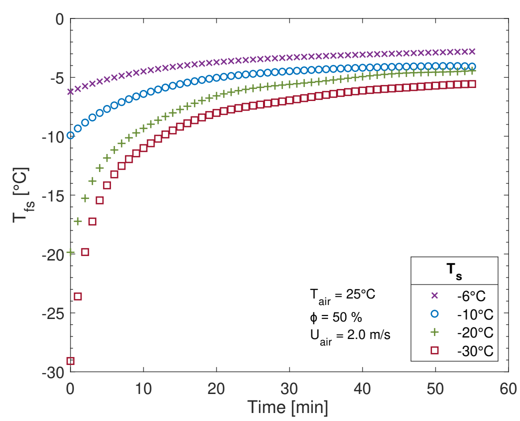

(c)

Figure 17: Calculated frost surface temperatures and their variations in time.

approach as shown in Eq. (24):

$$R_{cond}(t) = \frac{\delta_{outer}(t)}{k_{new}} + \frac{\delta_{inner}}{k_{old}(t)} \tag{24}$$

where,

$$\delta_{tot} = \delta_{inner} + \delta_{outer} \tag{25}$$

In this approach, the total frost layer is divided into inner and outer layers. By inner layer it is meant that the frost that was deposited within the first 20 min of the experiment (k_{old}). By the outer layer frost that is deposited after that time is considered (k_{new}). Checking the surface temperature variations after 20 min, a relatively small change in the surface temperature is seen, indicating majorly constant frost properties at the outer layer. That is why in Eq. (24) the thermal conductivity of the frost at the outer layer is taken as constant. On the other hand, the thickness of the inner layer is constant, but the heat conductivity of the inner frost layer is considered to be changing with time due to the densification process. Correspondingly, the rate of change in the total conduction thermal resistance in time is derived from Eq. (26) as:

$$\frac{dR}{dt} = \frac{1}{k_{outer}}\frac{d\delta_{outer}}{dt} - \frac{\delta_{inner}}{k_{inner}(t)^2}\frac{dk_{inner}(t)}{dt} \tag{26}$$

According to Eq. (26), the rate of change in the conduction thermal resistance depends on the frost thickness growth rate and as well as on the rate of change in the thermal conductivity of the inner frost layer. The first term on the right hand side represents the increase in conduction thermal resistance of the frost layer due to the growing outer layer. On the other hand, the second term could be attributed to the densification of the inner frost layer, driven by the water vapor diffusion towards the inner frost layer. In accordance with that, its sign is negative and reduces the total conduction resistance of the frost.

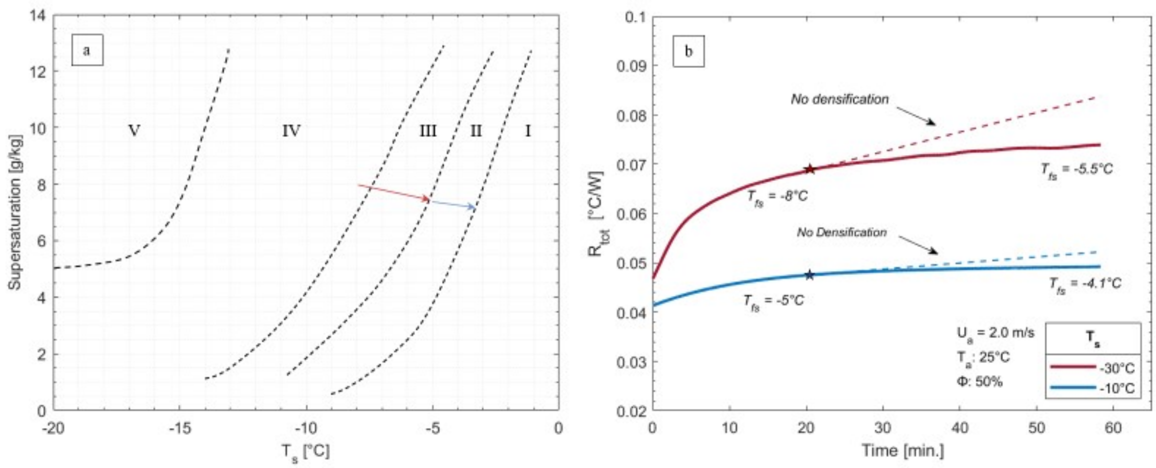

Figure 18: (a) Ice crystal shapes topography [1](b) Comparison of total thermal resistances with and without the presence of internal frost densification.

Figure 18 shows the increase in the total heat transfer resistance at the cold surface temperatures of between -10 and -30°C. The dashed lines drawn tangent to the resistance curves represent what the resistance increase would be if there was no densification of the inner frost layers which is expressed by the second term of the right hand side of Eq. (26) In this methodology, the change in the thermal properties of the outer frost layer was neglected. This is due to the fact that the frost surface temperature variations after the 20 min of the experiment are much less compared to the initial frost accumulation stage. Secondly, the frost ice crystal shapes at the outer frost layer that is formed after the 20 min of the experiment is also constant. Wu et al. [1] characterized the formed ice crystal shapes based on the temperature and amount of supersaturation. The presented chart was divided into five regions considering different ice crystal shapes. For both surface temperatures, the evaluation of the conditions at the frost surface during the 40 min of the experiments are mapped on the plot. As shown, the ice crystal shapes do not change during the next 40 min of the experiment which justifies the assumption of neglecting the temporal change in the thermal conductivity of the outer frost layer.

Comparing the cases with two different cold surface temperatures, one can see that densification has a much more pronounced effect on the thermal resistance at the surface temperature of −30°C. Quantitatively, the gain in the conductivity due to the densification is about 10 times more at the surface temperature of −30°C compared to the case at the surface temperature of −10°C. The pronounced effect of the densification process on the thermal resistance at colder surface temperatures could be due to the larger temperature difference across the inner frost layer which promotes the humidity diffusion into the inner frost layer.

4.7 Heat Flux Correlation

Using the experimental data, a correlation for heat flux was derived. For that purpose, the heat flux and temperature data were utilized in their dimensionless forms as:

$$q^* = \frac{q''_{min} - q''(t)}{q''_{min} - q''_{t=0}} \tag{27}$$

Here, $q"_{min}$ is the minimum heat flux that would be reached when the frost surface temperature reaches to 0°C, and no more frost formation occurs. Furthermore, $q"_{t=0}$ is the initial heat flux at the start of the frosting process and q"(t) is the instantaneously recorded heat flux. According to this definition, q* always starts at 1 at the beginning of the frosting regardless of the experimental conditions and decays towards zero as the frost surface temperature approaches to 0°C. Similarly, a non-dimensional temperature T* is also used as:

$$T^* = \frac{T_{air} - T_{tp}}{T_{air} - T_s} \tag{28}$$

Accordingly, a correlation for heat flux drop during the frost formation was proposed as a sum of two exponential functions as given in Eq. (29):

$$q^* = a\left(\frac{T_a}{0.45}\right) exp\left[bFo\left(\frac{Re}{10000}\right)^c\right] + d\left(\frac{T_a}{0.45}\right) exp\left[eFo\left(\frac{Re}{10000}\right)^c\right] \tag{29}$$

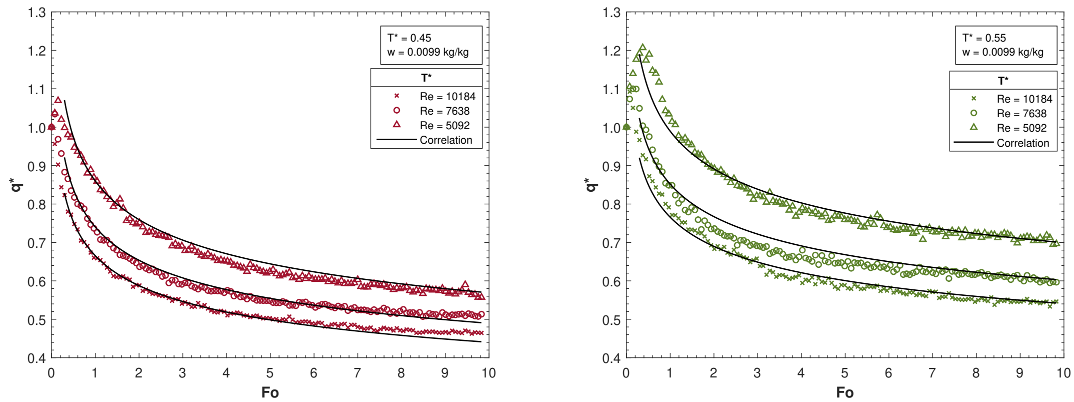

(a) (b)

Figure 19: Comparison of proposed correlation and experimental data.

when

$$0.45 < T_a < 0.55$$

$$5092 < Re < 10184$$

$$\text{w} = 0.0099 \text{ kg/kg}$$

where a = 0.53, b = -1.413, c = 2, d = 0.43, e = -0.05

Figure 19 shows the comparison of derived correlation along with the experimental data. Proposed correlation shows a good agreement with the experimental measurements, especially under the conditions where initial rise in the heat flux is less pronounced. However for the T* values greater than or closer to 0.55, proposed model deviates from the measured data since it is unable to capture initial heat transfer rise.

CHAPTER V

NUMERICAL RESULTS

In this chapter, the systematic approach for tuning the model parameters is explained. Next, the simulation results are discussed by comparing them with the experimental data.

5.1 Tuning the Model Parameters

As described in the numerical model section, τ is one of the parameters controlling the frost mass source term. This parameter has a dominant role on the frost deposition rate especially at the initial phase of the experiment where there was no prior frost accumulation on the surface. With time, frost thickness increases, and other factors such as the frost thermal conductivity, porosity, humidity diffusion through the porous frost layer starts to play a more dominant role in frosting process. Accordingly, the frost mass accumulation rate becomes insensitive to τ parameter with increasing frost thickness. Because of this reason, for the tuning of τ parameter only the initial phase of the experimental data was utilized where the sensitivity of the frosting on this parameter is highest. However, since there was no measurable frost thickness data at the initial phase of the experiment, the surface heat flux data was used for the tuning of τ parameter. Figure 20 shows the effect of different τ constants on the initial heat flux when there was no prior frost accumulation on the surface. At first, the surface temperature is set to -20°C and the initial 6 readings of experimental and numerical heat flux data were plotted for different τ constants considered. Accordingly, 80 was found to be closest to the experimental data for that temperature condition. Also, the validity of the selected τ value is tested for a different surface temperature of -30°C and shown in the same plot. As shown, calculations where τ was set to 80 can

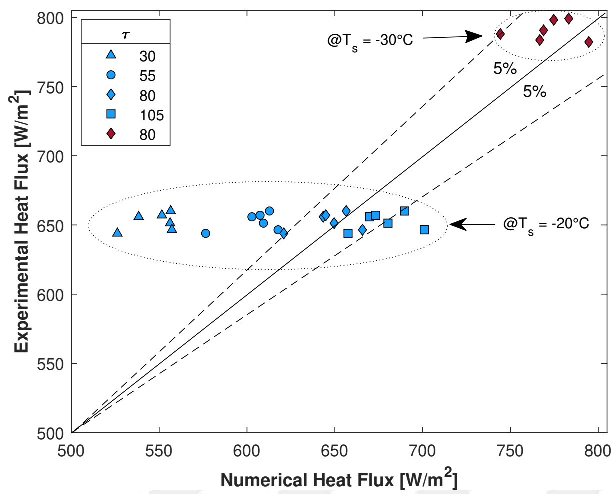

Figure 20: Comparison between the initial experimental and numerical heat flux data for different τ values

predict the experimental heat flux data with less than 5% error for both considered temperatures. Thus, τ was set to 80 in the further numerical simulations and the value of τ was kept constant during the entire duration of the frosting process.

As mentioned in the numerical method section, humid air velocity inside the thermal boundary layer and inside the porous frost layer plays an important role in the frosting process. Experimental results showed that frosting only occurs at the surface, and later ice crystal growth takes place over the existing frost layer. Even though the humid air temperature above the cold surface is low enough, no frost formation was observed in air. This could be due to the absence of nucleation sites in the air that could initiate frost formation. To include this mechanism into the frosting model a humid air velocity dependent parameter κ was added into the frost mass source term. First, this parameter was considered as a step-function type parameter as specified in Eq. (30). According to that, frosting is only allowed when the humid air velocity is below the defined velocity threshold, u_{lim}.

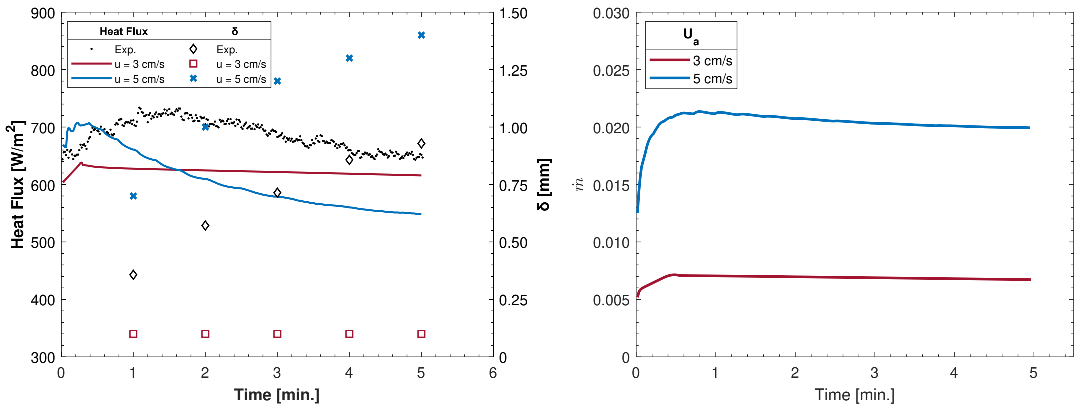

(a) (b)

Figure 21: Effect of the thickness growth parameter, κ.

$$\kappa_{u_{ha}} = \begin{cases} 1, & u_{ha} < u_{lim} \\ 0, & u_{ha} > u_{lim} \end{cases} \tag{30}$$

The effect of the different velocity threshold levels on the predicted heat flux and on the accumulated frost thickness is next checked. Two different threshold levels that are 3 cm/s and 5 cm/s were tested. The resulting thickness and heat flux levels are shown in Figure 21. As shown, having a threshold value of 3 cm/s severely underpredicts the experimental frost thickness. On the other hand, the threshold value above 5 cm/s overpredicts the frost thickness. Similarly, there is also a considerable difference in the predicted mass flow rates between these two cases. However, even though the threshold level had a major influence on the frost thickness and on the frost mass, it had a relatively weak influence on the heat flux levels. Results show that a higher velocity threshold level results in a higher heat flux level at the initial phase of the frosting. However, with time the increase in the frost thickness results in a drop in the heat flux level. However, in the case with a lower threshold value a constant heat flux level is preserved due to the non-growing frost thickness over time.

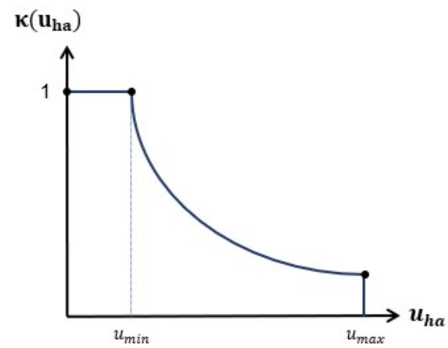

Figure 22: The A constant is determined according to the humid air velocity.

Based on these findings one may conclude that using a threshold level that falls right in-between those two levels could be reasonable. In this study, a slightly different approach was followed. Accordingly, instead of using a discontinuous step type function a continuous type limiter function was utilized. The function shown in Eq. (31) takes benefit of two threshold levels instead of one. And for humid air velocities that fall between these two threshold levels κ is calculated by an exponential decay type of function.

$$\kappa_{u_{ha}} = \begin{cases} 1, & u_{ha} < u_{lim} \\ e^{-M(u_{ha}-u_{min})}, & u_{ha} > u_{lim} \\ 0, & u_{ha} > u_{lim} \end{cases} \tag{31}$$

The behavior of this piecewise function is shown in Figure 22.

Figure 23, shows the results obtained with the discussed velocity dependent parameter κ. In comparison to the predicted frost height, a much better agreement with the experimental frost thickness was captured. Also, the new κ parameter function predicts the heat flux much closer than the previous ones. Especially, the agreement after the first minute of frosting got much closer to the experimental data.

Furthermore, it was found that κ factor has also significant impact on the frost porosity levels. As shown in Figure 23, even though two different κ parameters result

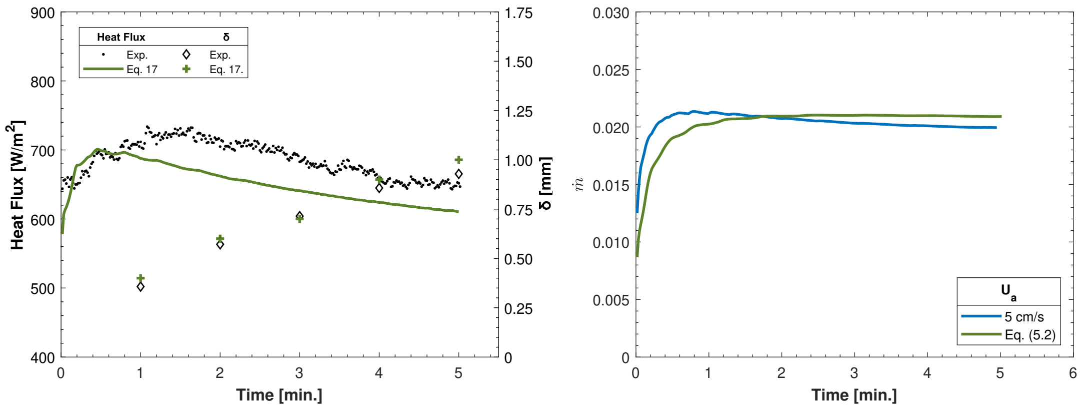

(a) (b)

Figure 23: Estimated heat flux and frost thickness by using Eq. (31). Similar frost mass is obtained compared to u=5 cm/s condition.

in a similar frost mass accumulation rate, the predicted frost thickness levels between these two cases are quite different from each other. This indicates that the porosity levels between these two cases must differ from each quite considerably. Having a reasonable match both in the predicted frost thickness and in the predicted heat flux levels, κ parameter given in Eq. (31) is used in further simulations.

5.2 Modeling Frost Thermal Conductivity

Frost is known to have a porous structure. Air trapped inside the frost layer can significantly lower the thermal conductivity of frost in comparison to solid ice. In addition to that, frost includes dendritic type ice crystals and their morphology inside the frost layer also affects the effective thermal conductivity of frost. However, in Euler-Euler multiphase modeling approach the exact shape of the ice crystals is not resolved but only the average ice volume fraction is calculated. This requires use of effective thermal conductivity models for the solid phase for the calculation of the conductive heat flux in the energy equation. Accurate prediction of the thermal conductivity of the solid frost layer can have a major influence on the frost thickness and on heat transfer to the substrate. To numerically test the approach, three different thermal conductivity approaches were used:

I. Thermal conductivity of frost is set equal to that of solid ice (2.2 W/m^2-K.) In this approach, the ice crystals were assumed to grow completely vertically from the bottom plate without any lateral branching. In this case heat transfer between the bottom plate and the frost top surface can be modeled with a parallel thermal resistance network.

II. Thermal conductivity of frost is set equal to that of humid air. In this approach, ice crystals were assumed to grow with heavy lateral branching. In this case heat transfer between the bottom plate and the frost top surface can be modeled with a serial thermal resistance network.

III. In addition to these models which consider the two extreme approaches for the frost thermal conductivity, the empirical model of Negrelli [40] is considered. This model considers both the vertical column-wise growth and branching of the ice crystals. This corresponds to a 1D thermal resistance network where the solid ice and humid air phases are arranged in a way that the total thermal resistance is higher than the parallel network arrangement but lower compared to the serial network arrangement. This approach is the closest to real case compared to previous two approaches, since an ice crystal might grow in any direction constituting a combination of series and parallel configurations. The proposed correlation for this approach is given in Eq. (32)

$$k_f = k_i a \left(\frac{k_a}{k_i}\right)^{b(1-\alpha_i)} \tag{32}$$

The previously explained three growth types were shown in 24.

To further clarify the issue, computational experiments were performed in order to show the effect of cell volume fraction distribution to heat flux and frost thickness. To

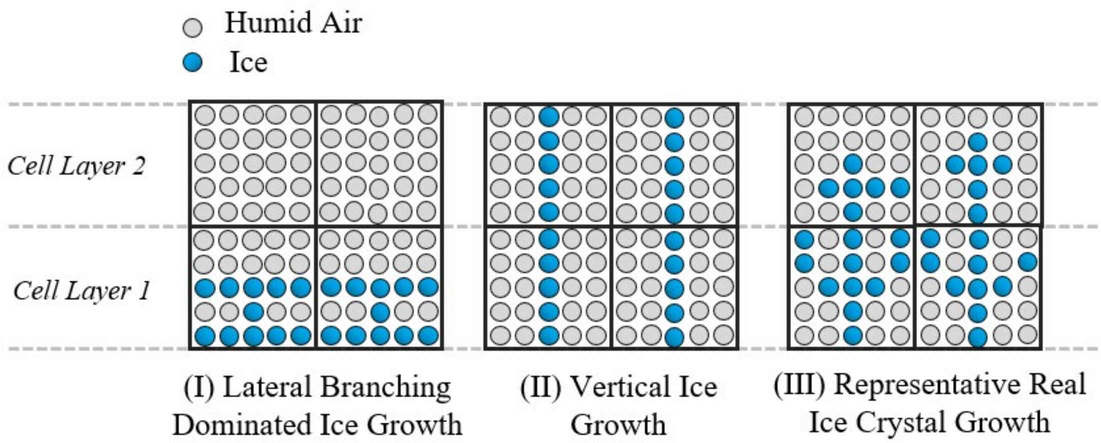

Figure 24: The distribution of a secondary ice phase in a cell. (I) Series type growth (II) Parallel type growth (III) A representative ice crystal.

do so, firstly two extreme cases of full series and parallel orientation were tested and results were compared against an experimental data. To mimic the full series case, the ice phase thermal conductivity was inputted as air's thermal conductivity, which is approximately 0.023 W/m^2-K. Considering the minor variation of thermal conductivity of frost layer for high porosity in series configuration, inputting air thermal conductivity is found a reliable approach to treat the secondary phase in series [40].

The validity of these different thermal conductivity models were next tested on a computational study. Figure 25 shows the predicted heat flux levels and frost thicknesses with the frost thermal conductivity models discussed above. As shown, the parallel type calculation of ice phase led to highest heat flux, and to the thickest frost layer. This thermal conductivity model induces the least thermal resistance between the surface and the frost surface and thereby results in the largest frost layer growth. A closer look at first three minutes of the data, one can see that this thermal conductivity model has the best match in heat flux among the three models. It captures the rise in the heat flux with the growing frost thickness. However, after that point it fails to predict the drop in heat flux that is observed at higher thickness levels. Moreover, it also overpredicts the frost thickness considerably.

On the other hand, the thermal conductivity model (II) yielded the lowest heat flux even though the predicted frost thickness was lowest among all. With this model frost stops growing after the first 15 min. of the simulation. Both thermal conductivity models (I) and (II) predict the frost height in the first 5 min. of the experiment quite well. However, from that point on the predictions of the models start to diverge.

The simulations results with the thermal conductivity model "(III)" by Negrelli [40] is also shown in Figure 25. Here, one can see that this model results to the best match with the experimental frost thickness. The heat flux distribution with this model is close to the prediction with the model "(II)". Even though, the final frost thickness levels at the end of 25 min are considerably different between model (III) and model (II), the predicted heat flux levels are almost the same.

To sum up, based on the simulation results, the best match with the heat flux data at the initial phase of the frosting process is reached with the thermal conductivity model (I) which uses the thermal conductivity of the solid ice for the frost phase. So, one can deduce that the ice crystal predominantly grows vertically in a column-like shape without considerable lateral branching in the initial phase of the process. It is also important to mention that different thermal conductivity models predict very similar frost thickness levels in the first 5 min. of the process. The insensitivity of the predicted frost thickness levels at the early stages of the process indicates the difficulty of validating frost models utilizing only frost thickness data. However, at the later stages of the process a clear difference in the predicted frost thickness levels is observed. Results also show that the thermal conductivity model (I) severely overpredicts both heat flux and frost thickness. This indicates a reduction in the thermal conductivity of the frost that forms after the first 5 min. of the process. One can conclude from that the frost layer forming at the later stages of the process might show a much higher branching compared to the frost that had already formed. Finally, considering its accuracy on frost thickness and also on the heat flux, the frost

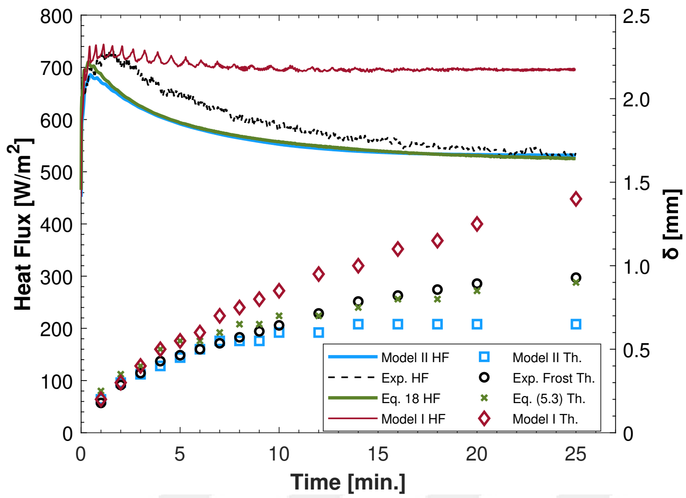

Figure 25: Heat Flux and frost thickness comparison concerning different cell volume fraction distributions.

thermal conductivity model [40] is used in the remaining part of this study.

5.3 Effect of Diffusion Coefficient over Frosting

The effect of the frost mass source term and the frost thermal conductivity on the process were discussed so far. Another significant factor that might influence the frosting process is the diffusion coefficient of the water vapor which controls the water vapor mass transfer into the frost layer. This coefficient could have a considerable effect on the frost accumulation and also on the heat transfer rate to the surface. When the boundary layer on the surface is laminar then the mass transfer to the surface is only governed by diffusion. However, the rough frost surface can trigger local eddy dominated flow patterns in the boundary layer which would require a very high resolution numerical model to capture. However, the effect of these local eddies can be artificially modeled with an increase in the molecular diffusion coefficient. This would correspond to adding eddy viscosity via a turbulence model for the modeling of turbulent flows.

Figure 26 shows the results of the simulations using three different diffusion coefficients. In addition to the simulation with the real diffusion coefficient D = 2.88

x $10^{-5} m^2$/s, an additional simulation with higher diffusion coefficient were also conducted. Results show that, frost thickness is quite insensitive to the diffusion coefficient. On the other hand, diffusion coefficient has a considerable effect on the heat flux levels and on the frost mass flow rates. Simulation with increased diffusion coefficient captures the heat flux rate at the initial stage of frosting relatively well. However, it also overpredicts the heat flux at the later stages of the process. The heat flux levels at the later stages of the frosting process is best predicted using the real diffusion coefficient in the simulations but that one is also underpredicts the heat flux at the early stages of the process. The improved prediction of the initial heat flux level with the increased diffusion coefficient might indicate the turbulent character of the boundary layer at least at the initial stage of the process. The rather sharp frost crystals formed at the inital stage of the process is expected to increase the surface roughness which might enhance mass transfer from the free stream into the boundary layer by turbulent mixing. However, at the later stages of frosting the frost surface becomes smoother which might inhibit the eddy dominated mixing that could have been present when the frost surface was rough. In addition, the result might signal the need for a turbulence model that would capture the turbulent mixing at the initial stages of the frosting.

5.4 Extension Different Experimental Cases

The validity of the developed model was next tested on a test case scenario with different cold surface temperature than the one used for the tuning of the model parameters Figure 27 shows the results considering two different cold surface temperatures. Accordingly, decrease in heat flux during the frost layer growth was captured closely against the experimental data for both considered cases. Initially, heat flux rises in the early stage of frosting, which was also measured experimentally. The increase in the heat flux rate at the initial phase of the process could be due to the

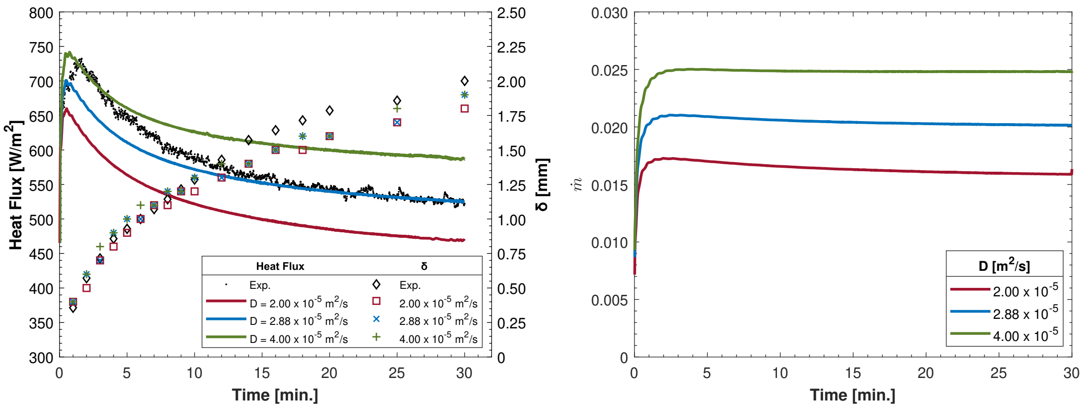

(a) (b)

Figure 26: Effect of diffusion coefficient, D on frosting. The water vapor diffusion in the air is 2.88 x 10^{-5} m^2/s at the room temperature.

rise in the available surface area with the growing ice crystals. That increases the total area where frost can accumulate. The increased frosting mass flow rate also results in more latent heat release from the growing ice crystals which is transferred to the cold surface. Over the duration of the process the frosting mass flow rate and the associated latent heat release rate seems to keep constant as shown previously in Figure 26. Later, the heat flux diminishes due to the decrease in the sensible heat flux over the frost surface. After 20 min, the drop in the heat flux rate is much lower than at the initial stages.

Furthermore, frost layer's thickness was also calculated during the simulations. Numerical solutions closely approximate the experimental data within the first 30 min. of simulation. Then, the applied models underpredict the thickness of the frost layer at both experimental conditions. After an hour, the model predicts the frost thickness about 5 mm lower than what it is in the measurement.

Figure 28 shows the evolution of the humid air temperature profile above the cold plate. The position of the frost surface is also marked on the profiles. As shown, within the first 5 min. of the frosting process the frost surface temperature shows a considerable rise. However, from this time onwards a very mild increase in the frost

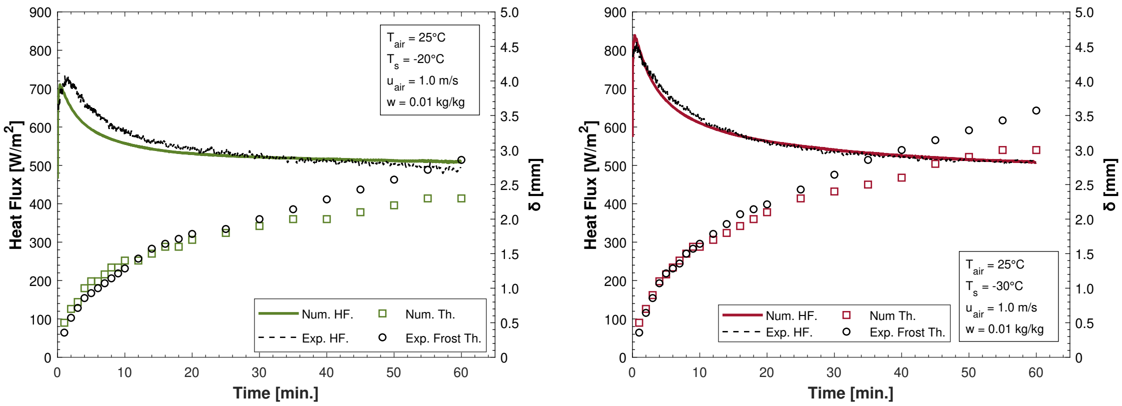

(a) (b)

Figure 27: Heat Flux and frost thickness comparisons for the tested cases.

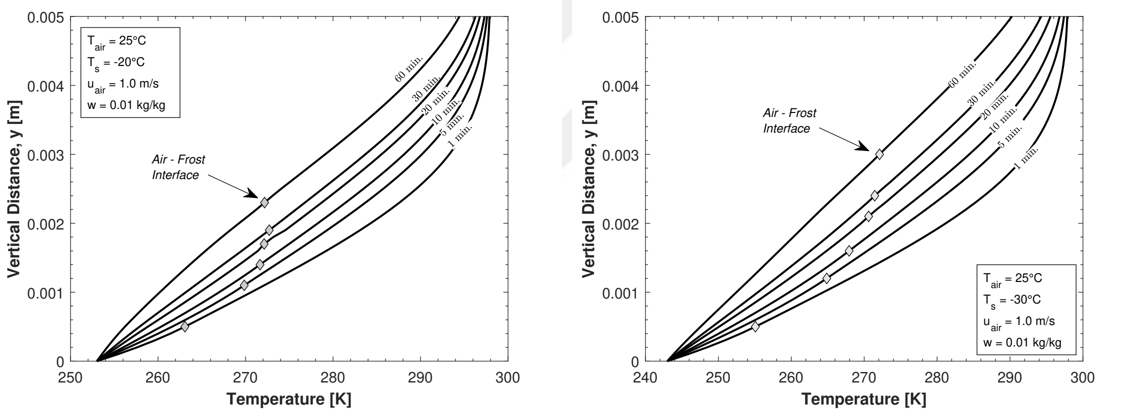

(a) (b)

Figure 28: Temperature profiles across the frost layer and its change in time.

surface temperature was observed. At the end of 60 min, the frost surface temperature reached to about -3°C in both simulations

The change in the thermal conductivity of the frost layer is illustrated in Figure 29. Comparing the two cases, the frost layer is found to be thermally less conductive when the cold surface temperature is lower. The highest conductivity is obtained in the regions close to cold plate for each time interval, since frost is denser there. Also, frost layer conductivity continuously increases with the frost mass accumulation on the surface which rises the frost density.

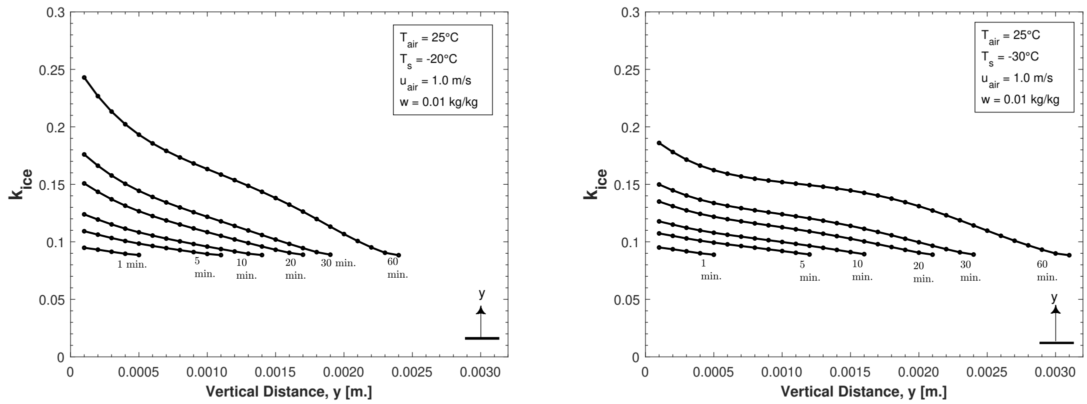

(a) (b)

Figure 29: Thermal conductivity distribution across frost layer.

Figure 30 shows the evolution of frost mass generation rate across the frost layer. For the simulation with the surface temperature held at -20°C higher frosting rates were observed closer to the cold surface within the first 20 minutes. However, in the later stages of the process the frosting rate distribution started to be more uniform across the frost layer. Towards the end of the simulation, the more enhanced frosting was observed towards the frost top surface. In other words, the region with the highest mass accumulation rate, shifts from the cold plate region to the air – frost interface. For the case with the surface temperature held at -30°C, phase change seems to be more uniform across the frost layer. However, in this case the frost accumulation rate enhances towards the frost top surface at the final stages of the simulation.

Volume fraction profiles through the frost layers are illustrated in Figure 31. Results show a denser frost structure closer to the cold surface in both simulations. Also, it is observed that a denser frost layer was found at the simulation with -20°C surface temperature compared to the frost formed at the surface held at -30°C. The simulation with the surface temperature held at -30°C yielded a thicker and more porous frost layer which eventually led to a more pronounced decrease in the heat transfer.

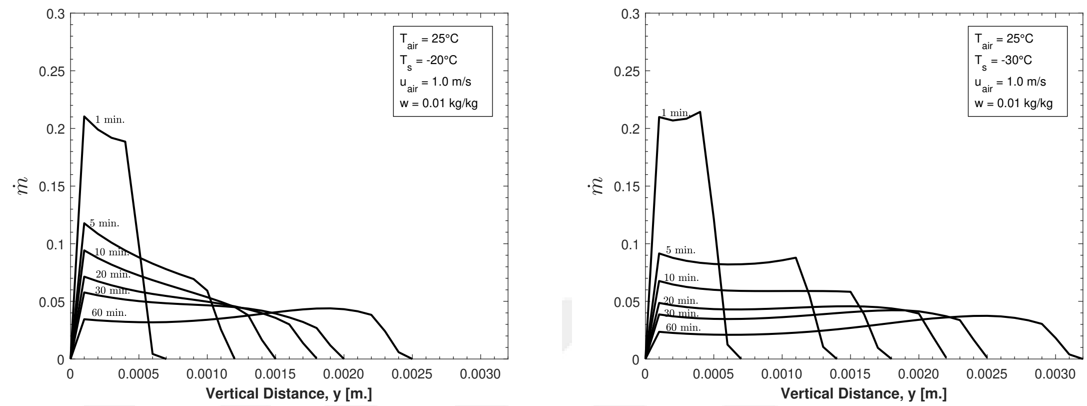

(a) (b)

Figure 30: The amount of mass generated for frosting.

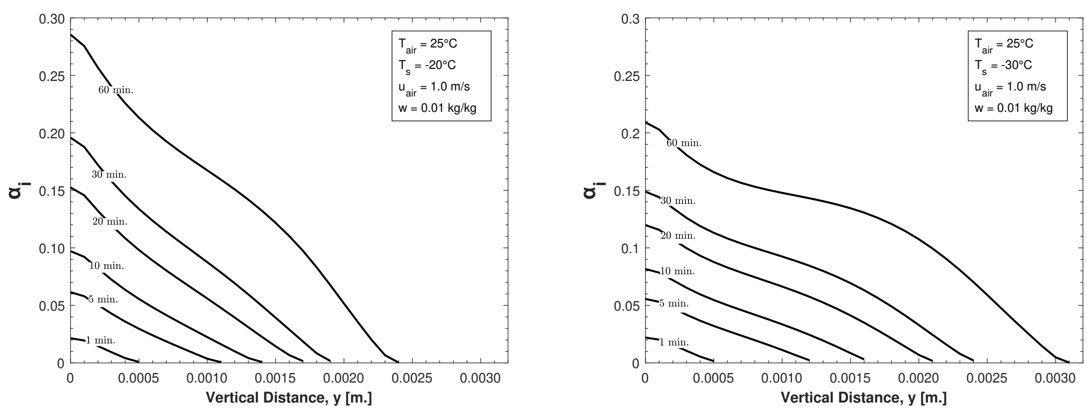

(a) (b)

Figure 31: Volume fraction distribution of ice across the frost layer.

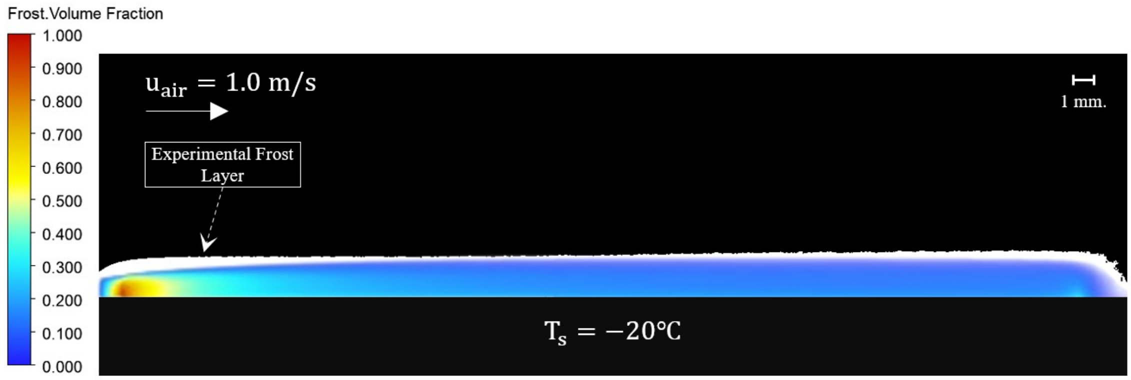

Figure 32: Comparison between numerical and experimental frost layer at the end of the simulation.

Figure 32 compares the numerically predicted frost layer with the experimental frost layer. Accordingly, the model closely predicts the frost thickness at the center of the cold surface. However, it is less successful in predicting the frost thickness at the leading edge. The present model also predicts a denser frost structure at the leading edge which was also reported by the previous studies [28, 29].

CHAPTER VI

CONCLUSIONS

In this study, the effect of frosting on heat transfer is experimentally investigated. The data gathered from the experiments were utilized to develop a numerical model to calculate dynamic heat transfer rates over a horizontal plate under frosting conditions. The following conclusions were drawn from the experimental measurements:

I. In most of the considered experimental conditions, especially at low cold surface temperatures, considerable drops in the convective heat flux levels were measured as soon as frosting process starts. The rate of decrease in the heat flux was not found to be constant. Initial drop in the heat flux within the first 20 minutes of the experiment was found to be much more pronounced.

II. The measured total heat flux is due to both the latent and sensible heat fluxes. Heat flux induced by the latent heat remains nearly unchanged during experiments. On the other hand, sensible heat flux showed a more pronounced reduction due to the rise in the frost surface temperature during the duration of frosting.

III. At low air velocities and at high cold surface temperatures an initial rise in the heat transfer was observed. This effect got even more pronounced as the air velocity is reduced. Considering the spiky frost surface at low air velocities it is anticipated that the heat flux rise at the initial stage of the frosting could be due to the heat transfer area increase similar to the way the fins enhance heat transfer, and a subsequent increase in the frosting rate and latent heat release.

IV. Densification of the frost layers was found to have a considerable effect on the total thermal resistance. This effect was found to be more pronounced at low cold surface temperatures.

V. A heat flux drop correlation due to the frost formation was developed. Using this correlation, the decrease in the heat transfer could be estimated.

Based on the obtained empirical data, a new modeling approach was developed and implemented to a commercial software. An Euler-Euler based multi-phase numerical model was developed to numerically investigate frost formation process over flat cold surface. In the developed model, frost accumulation over the flat surface is modeled by an empirical mass source term requiring experimental data for the determination of the source term model constants. In the present study, a velocity dependent coefficient is introduced into the mass source term model which considerably increased the accuracy of the model, especially at the initial stages of frost growth. The constants in the mass source term are tuned in a systematic approach using both the experimental frost thickness and heat flux data. To the best of author's knowledge, for the first time in the literature, a multi-phase frost model was developed that can predict both the accumulated frost thickness and heat flux to the cold surface. The key aspects of the present model and main findings from the simulation results are:

I. A velocity dependent coefficient was introduced into the frost mass source term model. This term scales the frost formation based on the local humid air velocity. With the introduction of this term, the accuracy of the model in the prediction of the heat flux and of frost thickness growth at the initial stages of frosting is considerably increased.

II. Three different frost layer thermal conductivity models were considered and their effects on the surface heat flux and frost thickness growth were investigated. Simulation based heat flux results show that the frost formed at the early stages of the process has a thermal conductivity very close to that of solid ice. This indicates that ice crystal growth at the early stage of frosting predominantly occurs in the longitudinal direction. However, the decrease in the heat flux data with increasing frost thickness at the later stages of the process was best predicted with the thermal conductivity model by Negrelli et al. [40]. This indicates that, the frost layers formed at the later stages of the process might be composed of ice crystals with increased lateral branching.

III. The increase in the heat flux at the early stage of frosting was captured numerically with the aid of the proposed model. The increase was attributed to the rise in the available heat transfer area at the early stage, which facilitates more nucleation sides for desublimation. As a result, latent heat release becomes more abundant at the initial duration of frosting, contributing to the total heat transfer rates.the total thermal resistance. This effect was found to be more pronounced at low cold surface temperatures.

IV. Simulations conducted with increased diffusion coefficient for water vapor considerably increased both the heat flux onto the cold surface and frost mass accumulation on cold surface. So, the rise in the heat flux at the early stages of frosting is much better captured with the increased diffusion coefficient. Considering that a laminar flow model was used in all simulations, the improved accuracy with the increased diffusion coefficient might indicate an eddy-driven mass transport into the frost layer due to a possible turbulent flow regime at the boundary layer on the frost layer.

V. Simulation results with the cold surface temperature at -30℃ resulted to a more porous frost layer compared to the simulation with the cold surface temperature of -20℃. The increased porosity observed with the lower surface temperature results from an increased frost growth rate.

CHAPTER VII

RECOMMENDATIONS FOR FUTURE RESEARCH

The research that is carried out in this thesis can be extended to investigate frosting phenomenon further. Some of the recommended future research goals were listed in below:

I. The existing experimental setup could be utilized to conduct more frosting experiments. So that, the proposed correlation can be modified for a broader span. Especially, air temperature regimes closer to 0ºC can be priority.

II. The experiments could be performed not only keeping the aforementioned parameters constant during the experiments, but also variable surface temperature and air velocity conditions could be employed to mitigate the frosting effects on heat transfer. These parameters could be set variably during an experiment. So that, strategies could be devised to attain highest average heat transfer rates under frosting situation.

III. The experimental setup can be modified to mount an evaporator section, and carry out frosting experiments under controlled ambient conditions. Furthermore, by positioning a heat flux sensor between the outlet and inlets of evaporator, real time heat transfer decrease could be measurable by means of induced temperature difference in the refrigerant due to frosting.

IV. The proposed numerical approach can be tested under different environmental conditions. Various air velocities, air temperatures, air humidity levels and cold surface temperatures are the primary parameters that the validity of the model could be tested. The model parameters can be tuned and linked to empirical findings accordingly.

V. The numerical model could be tested for different geometries to calculate heat transfer rates under frosting. Especially, finned geometries should be considered. A 2-D numerical domain can be configured for that purpose, and frosting between two parallel plates representing flow between an evaporator of fins can be modeled Accordingly, decrease in heat transfer and air blockage due to frosting can be calculated.

REFERENCES

[1] X. Wu, W. Dai, W. Xu, and L. Tang, "Mesoscale investigation of frost formation on a cold surface," *Experimental Thermal and Fluid Science*, vol. 31, no. 8, pp. 1043–1048, 2007.

[2] J. Yonko and C. Sepsy, "An investigation of the thermal conductivity of frost while forming on a flat horizontal plate," *ASHRAE Trans.*, vol. 73 (II), pp. 1.1–1.11, 1967.

[3] H. Auracher, "Effective thermal conductivity of frost," *Proceedings of the Int. Symp. Heat Mass Transfer*, pp. 285–301, 1987.

[4] Y. Hayashi, A. Aoki, S. Adachi, and K. Hori, "Study of frost properties correlating with frost formation types," *Journal of Heat Transfer*, vol. 99, no. 2, p. 239–245, 1977.

[5] B. Na and R. L. Webb, "New model for frost growth rate," *International Journal of Heat and Mass Transfer*, vol. 47, no. 5, pp. 925–936, 2004.

[6] S. Negrelli and C. J. Hermes, "A semi-empirical correlation for the thermal conductivity of frost," *International Journal of Refrigeration*, vol. 58, pp. 243–252, 2015.

[7] S.-M. Li, K.-S. Yang, and C.-C. Wang, "A semi-empirical model for predicting frost properties," *Processes*, vol. 9, no. 3, 2021.

[8] K.-S. Lee, W.-S. Kim, and T.-H. Lee, "A one-dimensional model for frost formation on a cold flat surface," *International Journal of Heat and Mass Transfer*, vol. 40, no. 18, pp. 4359–4365, 1997.

[9] K.-S. Lee, S. Jhee, and D.-K. Yang, "Prediction of the frost formation on a cold flat surface," *International Journal of Heat and Mass Transfer*, vol. 46, no. 20, pp. 3789–3796, 2003.

[10] R. Yun, Y. Kim, and M. ki Min, "Modeling of frost growth and frost properties with airflow over a flat plate," *International Journal of Refrigeration*, vol. 25, no. 3, pp. 362–371, 2002.

[11] M. Kandula, "Frost growth and densification in laminar flow over flat surfaces," *International Journal of Heat and Mass Transfer*, vol. 54, no. 15, pp. 3719–3731, 2011.

[12] Y. L. Hao, J. Iragorry, and Y.-X. Tao, "Frost-Air Interface Characterization Under Natural Convection," *Journal of Heat Transfer*, vol. 127, pp. 1174–1180, 04 2005.

[13] R. Östin and S. Andersson, "Frost growth parameters in a forced air stream," *International Journal of Heat and Mass Transfer*, vol. 34, no. 4, pp. 1009–1017, 1991.

[14] A. Z.Şahin, "An experimental study on the initiation and growth of frost formation on a horizontal plate," *Experimental Heat Transfer*, vol. 7, no. 2, pp. 101–119, 1994.

[15] C.-H. Cheng and C.-C. Shiu, "Frost formation and frost crystal growth on a cold plate in atmospheric air flow," *International Journal of Heat and Mass Transfer*, vol. 45, no. 21, pp. 4289–4303, 2002.

[16] C.-H. Cheng and K.-H. Wu, "Observations of Early-Stage Frost Formation on a Cold Plate in Atmospheric Air Flow ," *Journal of Heat Transfer*, vol. 125, pp. 95–102, 01 2003.

[17] C. J. Hermes, R. O. Piucco, J. R. Barbosa, and C. Melo, "A study of frost growth and densification on flat surfaces," *Experimental Thermal and Fluid Science*, vol. 33, no. 2, pp. 371–379, 2009.

[18] L. Huang, Z. Liu, Y. Liu, and Y. Gou, "Experimental study of frost growth on a horizontal cold surface under forced convection," *Journal of Mechanical Science and Technology*, vol. 24, no. 7, p. 1523–1529, 2010.

[19] A. Leoni, M. Mondot, F. Durier, R. Revellin, and P. Haberschill, "Frost formation and development on flat plate: Experimental investigation and comparison to predictive methods," *Experimental Thermal and Fluid Science*, vol. 88, pp. 220–233, 2017.

[20] D. O'Neal, *The Effects of Frost Formation on the Performance of a Parallel Plate Heat Exchanger*. PhD thesis, 1983.

[21] J. Lee, J. Kim, D. R. Kim, and K.-S. Lee, "Modeling of frost layer growth considering frost porosity," *International Journal of Heat and Mass Transfer*, vol. 126, pp. 980–988, 2018.

[22] B. W. Jones and J. D. Parker, "Frost Formation With Varying Environmental Parameters," *Journal of Heat Transfer*, vol. 97, pp. 255–259, 05 1975.

[23] C. J. Hermes, "An analytical solution to the problem of frost growth and densification on flat surfaces," *International Journal of Heat and Mass Transfer*, vol. 55, no. 23, pp. 7346–7351, 2012.

[24] B. Na and R. L. Webb, "Mass transfer on and within a frost layer," *International Journal of Heat and Mass Transfer*, vol. 47, no. 5, pp. 899–911, 2004.

[25] J. Cui, W. Li, Y. Liu, and Z. Jiang, "A new time- and space-dependent model for predicting frost formation," *Applied Thermal Engineering*, vol. 31, no. 4, pp. 447–457, 2011.

[26] J. Cui, W. Li, Y. Liu, and Y. Zhao, "A new model for predicting performance of fin-and-tube heat exchanger under frost condition," *International Journal of Heat and Fluid Flow*, vol. 32, no. 1, pp. 249–260, 2011.

[27] D. Kim, C. Kim, and K.-S. Lee, "Frosting model for predicting macroscopic and local frost behaviors on a cold plate," *International Journal of Heat and Mass Transfer*, vol. 82, pp. 135–142, 2015.

[28] J. Armengol, C. Salinas, J. Xamán, and K. Ismail, "Modeling of frost formation over parallel cold plates considering a two-dimensional growth rate," *International Journal of Thermal Sciences*, vol. 104, pp. 245–256, 2016.

[29] X. Wu, Q. Ma, F. Chu, and S. Hu, "Phase change mass transfer model for frost growth and densification," *International Journal of Heat and Mass Transfer*, vol. 96, pp. 11–19, 2016.

[30] X. Wu, Q. Ma, and F. Chu, "Numerical Simulation of Frosting on Fin-and-Tube Heat Exchanger Surfaces," *Journal of Thermal Science and Engineering Applications*, vol. 9, 04 2017.

[31] X. Wu, F. Chu, and Q. Ma, "Frosting model based on phase change driving force," *International Journal of Heat and Mass Transfer*, vol. 110, pp. 760–767, 2017.

[32] Q. Ma, X. Wu, F. Chu, and B. Zhu, "Experimental and numerical investigations of frost formation on wavy plates," *Applied Thermal Engineering*, vol. 138, pp. 627–632, 2018.

[33] C. Kim, J. Lee, and K.-S. Lee, "Numerical modeling of frost growth and densification on a cold plate using frost formation resistance," *International Journal of Heat and Mass Transfer*, vol. 115, pp. 1055–1063, 2017.

[34] S. Byun, H. Jeong, D. R. Kim, and K.-S. Lee, "Frost modeling under cryogenic conditions," *International Journal of Heat and Mass Transfer*, vol. 161, p. 120250, 2020.

[35] B. Sun, S. Ghatage, G. M. Evans, T. Bhatelia, R. P. Utikar, and V. K. Pareek, "Dynamic study of frost formation on cryogenic surface," *International Journal of Heat and Mass Transfer*, vol. 150, p. 119372, 2020.

[36] Y. You, S. Wang, W. Lv, Y. Chen, and U. Gross, "A cfd model of frost formation based on dynamic meshes technique via secondary development of ansys fluent," *International Journal of Heat and Fluid Flow*, vol. 89, p. 108807, 2021.

[37] Z. Xu, Z. Wang, Z. Liang, H. Chen, and Z. Han, "A frost model based on the frost layer's supporting function," *International Journal of Heat and Mass Transfer*, vol. 202, p. 123741, 2023.

[38] J. C. Wong, V. K. Pareek, and B. Sun, "Cfd analysis of phase change behaviour and frost growth under various conditions using mass transfer theory," *International Journal of Heat and Mass Transfer*, vol. 198, p. 123396, 2022.

[39] E. Bartrons, P. A. Galione, and C. D. Pérez-Segarra, "Fixed grid numerical modelling of frost growth and densification," *International Journal of Heat and Mass Transfer*, vol. 130, pp. 215–229, 2019.

[40] S. Negrelli, R. P. Cardoso, and C. J. Hermes, "A finite-volume diffusion-limited aggregation model for predicting the effective thermal conductivity of frost," *International Journal of Heat and Mass Transfer*, vol. 101, pp. 1263–1272, 2016.

[41] N. Zgheib, M. Farzaneh, S. Balachandar, and S. Sherif, "A physics-based model for frost buildup under turbulent flow using direct numerical simulations," *International Journal of Heat and Mass Transfer*, vol. 182, p. 121915, 2022.

[42] M. Farzaneh, N. Zgheib, S. Sherif, and S. Balachandar, "Sensitivity analysis of frost deposition in turbulent flow over a cold plate using direct numerical simulation," *International Journal of Heat and Mass Transfer*, vol. 196, p. 123233, 2022.

[43] J. Gong, J. Hou, G. Li, T. Gao, and J. Sun, "A lattice boltzmann study of frost growth on a cold surface," *International Communications in Heat and Mass Transfer*, vol. 98, pp. 116–124, 2018.

[44] R. J. Moffat, "Describing the uncertainties in experimental results," *Experimental Thermal and Fluid Science*, vol. 1, no. 1, pp. 3–17, 1988.

[45] K. G. Libbrecht, "The physics of snow crystals," *Reports on Progress in Physics*, vol. 68, p. 855, mar 2005.

[46] J. Marti and K. Mauersberger, "A survey and new measurements of ice vapor pressure at temperatures between 170 and 250k," *Geophysical Research Letters*, vol. 20, no. 5, pp. 363–366, 1993.

[47] W. E. Ranz and J. W. R. Marshall, "Evaporation from drops, part i and part ii," *Chem. Eng. Prog*, vol. 48, pp. 173–180, apr 1952.

[48] L. Schiller and Z. Naumann, "A drag coefficient correlation," *VDI Zeitung*, vol. 77, pp. 318–320, 1935.

[49] Y. A. Cengel and A. J. Ghajar, *Heat and mass transfer: Fundamentals and applications*. McGraw-Hill Professional, 5 ed., 2014.

[50] "Experimental and numerical study of frost formation by natural convection over a cold horizontal circular cylinder," *International Journal of Refrigeration*, vol. 33, no. 7, pp. 1444–1458, 2010.